Article

HBV-associated hepatocellular carcinomas inhibit antitumor CD8+ T cell via the long noncoding RNA *HDAC2-AS2*

Yanan Gao[1,5], Zhenxing Zhang[1,5], Xuetao Huang[1,2,5], Maojun You [1,5], Chengzhi Du[1,2], Nan Li[3], Yajing Hao[1], Kang Wang[3], Xiang Ding[2,4], Fuquan Yang [2,4], Shu-qun Cheng [3], Jianjun Luo [1,2] ✉, Runsheng Chen [1,2] ✉ & Pengyuan Yang [1,2] ✉

Hepatocellular carcinoma (HCC) is one of the most common malignancies worldwide. Extracellular vesicles (EV) are critical mediators of intercellular communication within the tumor microenvironment, and cancer-cell-secreted EVs often facilitate cancer progression. Here we show that in HBV-associated HCC, tumor-cell-derived EVs contain a TGFβ-inducible long noncoding RNA, termed *HDAC2-AS2*. EVs enriched with *HDAC2-AS2* facilitate cancer progression by suppressing cytotoxicity of intra-tumor CD8+ T cells. Mechanistically, in activated cytotoxic CD8+ T cells, translocation of the transcription factor cyclin-dependent kinase 9 (CDK9), to the cytoplasm is critical for functional integrity. *HDAC2-AS2* targets and blocks cytosolic CDK9, and this results in exhaustion of PD-1+CD8+ T cells and suppression of IFN-γ+CD8+ T cell cytotoxicity. Notably, we demonstrate that low *CDK9* and high *HDAC2-AS2* expressions are associated with poor survival of HCC, which can be rescued by anti-PD-1 therapy. These findings emphasize the significance of tumor-derived EVs in suppressing antitumor CD8+ T cell immunity to promote tumorigenesis, and highlight extracellular *HDAC2-AS2* as a promising biomarker and therapeutic target for HCC.

Hepatocellular carcinoma (HCC) is one of the major and aggressive malignancies, ranking as the third leading cause of cancer-related mortality worldwide[1–3]. Due to the frequent diagnosis of HCC at advanced stages, postsurgical intrahepatic recurrence and extrahepatic recurrence intrahepatic metastasis result in a 5-year survival rate of <53%[4]. Chronic hepatitis B virus (HBV) and hepatitis C virus (HCV) infection are the major factors promoting the development and progression of HCC in most patients of eastern Asia, particularly among the Chinese population worldwide[5]. The HBV infection initiates inflammatory and fibrotic processes and induces extensive TGFβ and other cytokines production and leukocytes infiltration, thus creates a favorable microenvironment for HCC development[6]. Tumor-infiltrating lymphocytes (TIL) constitute an essential primary immune component of HCC and comprise a host antitumor reaction participant in immunotherapy treatment[7]. TGFβ signaling induces generation and infiltration of Treg cells, which impairs the effector function of CD8+ T cells and is associated with poor survival outcomes in HCC patients[8]. However, emerging evidence has indicated that the

[1]State Key Laboratory of Epigenetic Regulation and Intervention, CAS Center for Excellence in Biomacromolecules, Institute of Biophysics, Chinese Academy of Sciences, 100101 Beijing, China. [2]University of Chinese Academy of Sciences, 100101 Beijing, China. [3]Department of Hepatic Surgery VI, Eastern Hepatobiliary Surgery Hospital, Naval Medical University, Shanghai, China. [4]Laboratory of Proteomics, Institute of Biophysics, Chinese Academy of Sciences, Beijing, China. [5]These authors contributed equally: Yanan Gao, Zhenxing Zhang, Xuetao Huang, Maojun You. ✉e-mail: luojianj@ibp.ac.cn; rschen@ibp.ac.cn; pyyang@ibp.ac.cn

activated state of CD8$^+$ cytotoxic T lymphocytes (CTL), rather than just their presence, positively correlates with good prognosis[9,10]. Nevertheless, the dysfunction of cytolytic machineries and increased expression of inhibitory molecules (e.g., programmed cell death-ligand1, PD-L1) is believed to be responsible for the compromised tumor-specific killing by CD8$^+$ CTLs[11].

Long noncoding RNAs (lncRNA) are operationally defined as a class of transcripts that are longer than 200 nt with no or limited protein-coding potential[12]. Rapidly accumulating evidence suggests that lncRNAs play important roles in diverse biological processes involved in HCC progression, including proliferation, angiogenesis, invasion, and metastasis, through their interactions with other cellular RNAs, DNAs, and proteins[13–17]. On the other hand, several studies have also reported the involvement of lncRNAs in the development and function of human immune cells, including dendritic cells (DC), macrophages, and T cells[18–21]. For example, lnc-EGFR stimulates Treg cell differentiation and suppresses CTL activity, thereby promoting HCC growth in an EGFR-dependent manner[22]. NKILA lncRNA promotes tumor immune evasion by sensitizing TH1 and CTL cells to activation-induced cell death[23]. However, while these reported lncRNAs primarily functioned as cell-autonomous regulators within T cells, it is still largely unknown whether or how tumor-derived extracellular lncRNAs could influence TILs.

The discovery that extracellular vesicles (EV) can transport RNAs between cells suggests that extracellular RNAs (exRNA) may play previously unrecognized roles in intercellular communication, thereby launching the field of exRNA biology[24]. Importantly, recent studies have reported that tumor-derived EVs play crucial roles in modulating local and distant microenvironments, thus facilitating tumor escape from the host immune system and promoting tumor development[25–30]. Especially, studies have shown that tumor-derived EVs can deliver lncRNAs from glioblastoma or colorectal cancer cells to macrophages or natural killer (NK) cells to regulate the immune response[31,32]. However, whether lncRNAs delivered by EVs exert their influence on adaptive immunity, another important part of anti-tumor immunity has not been discussed.

In this study, we elucidate the impact of an extracellular lncRNA in linking CD8$^+$ T cells and HCC. We disclose that tumor-secreted lncRNA *HDAC2-AS2*, in response to TGFβ signaling activation, could be delivered into CD8$^+$ T cells to suppress antitumor immunity via tumor-derived EVs, consequently promoting HCC progression. These results highlight the importance of tumor-derived EV-delivered lncRNA in regulating tumor microenvironment for HCC development and provide a new biomarker and therapeutic target for HCC.

Results

HDAC2-AS2 is upregulated by TGFβ and correlates with poor survival of HCC

TGFβ signaling pathways play critical roles during liver pathogenesis, including chronic HBV/HCV infection, liver cirrhosis, and tumorigenesis[6,33,34], contributing to more immunotolerant microenvironment by upregulating functional RNAs and tumor-related signaling. Consistent with previous studies, *TGFβ1* is expressed at higher levels in HCC tissues than in noncancerous hepatic tissues (Supplementary Fig. 1a). To screen TGFβ-regulated lncRNAs, we treated a number of HCC cell lines with different metastatic potential (HepG2 and Huh7 cells, low metastatic potential; MHCC97 and PVTT cells, high metastatic potential) for 8 h and observed 46 downregulated and 121 upregulated lncRNAs (fold change ≥ 2, $p \le 0.05$) in the four treated cell lines via microarray analysis (Supplementary Fig. 1b). 11 candidates were further selected by comparing with TCGA database (TANRIC, fold change ≥ 1.5, $p \le 0.05$). The lncRNA, annotated as *HDAC2-AS2* (Ensembl ID: ENSG00000228624, fold change > 2, $p < 0.01$), stood out as the top candidate, which was further confirmed by mRNA detection (Fig. 1a).

HDAC2-AS2 resides on chromosome 6 with a full length of 776 nucleotides determined by 5′ and 3′RACE (rapid amplification of cDNA ends) assay (Supplementary Fig. 1c, Table S1). To clarify whether *HDAC2-AS2* can be upregulated by TGFβ signaling, we treated several HCC cell lines and normal liver cell line LO2 with TGFβ for 48 h and observed an increase in *HDAC2-AS2* expression (Fig. 1b). Either SB431542 inhibition or Smad4 knockout to block TGFβ signaling can abrogate *HDAC2-AS2* upregulation (Fig. 1c, d, Supplementary Fig. 1d). Since HBV infection can increase TGFβ secretion, we verified that *HDAC2-AS2* expressed higher in HepG2.2.15 (stable cell line integrating double-copy HBV genome in HepG2 cells) than parental HepG2 cells (Fig. 1e). In addition, using a HBV-infected HepG2-NTCP cell model[35], we found HBV infection significantly promoted the expression of *HDAC2-AS2* (Fig. 1f). *HDAC2-AS2* was highly expressed in clinical HCC samples compared with non-tumor tissues (Fig. 1g). Similar results were observed in TCGA database, not only in HCC, but also in STAD (stomach adenocarcinoma), KIRP (kidney renal papillary cell carcinoma) and KIRC (kidney renal clear cell carcinoma) tissues (Fig. 1h, Supplementary Fig. 2a).

Furthermore, we grouped the tumor and nontumor tissues sourced from the TCGA-LIHC database based on the etiology, and found that the tumors of HBV$^+$ HCC showed higher expression levels of *HDAC2-AS2* compared to nontumor tissues of HBV$^+$ HCC, tumor tissues of HCV$^+$ HCC and nonviral HCC (Fig. 1i). The expression of *HDAC2-AS2* was consistent with the *TGFB1* level, correlated with poor survival of HCC patients (Figs. 1j, S2b). We also grouped the tumor tissues obtained from TCGA-LIHC based on the *HDAC2-AS2* expression and performed differential expression analysis. *HDAC2-AS2* high-expressing tumor tissues exhibited elevated expression of 2147 genes (Supplementary Fig. 2c). Further GSVA analysis revealed that *HDAC2-AS2* high-expressing tumor tissues were enriched with signatures related to epithelial mesenchymal transition (EMT), lymphocyte mediated immunity, inflammatory response (Fig. 1k, Supplementary Fig. 2d). Collectively, these data demonstrate that HBV-TGFβ-upregulated *HDAC2-AS2* is elevated in tumor tissues and is associated with poor survival.

HDAC2-AS2 promotes tumor growth by affecting tumor microenvironment

To investigate the biological functions of *HDAC2-AS2* in HCC progression, we first identified that *HDAC2-AS2* showed no influence on its nearest gene *HS3ST5*, *HDAC2*, and *MARCKS* expression (Supplementary Fig. 3a, b). Then, we tested whether *HDAC2-AS2* could influence tumor cell growth in vitro. Both colony formation and sphere formation assays revealed no significant discrepancy in clone numbers and spheroid numbers (Supplementary Fig. 3c–e). A subcutaneous mouse model was also employed with a murine liver tumor cell line (Hepa1-6) to further explore *HDAC2-AS2* overexpression had no effect on both tumor growth and tumor weight in nude mice (Fig. 2a–c), demonstrating *HDAC2-AS2* did not affect tumor progression itself. Thus, the association between *HDAC2-AS2* and HCC may be mediated by tumor microenvironment (TME).

To verify this hypothesis, we wonder whether *HDAC2-AS2* might influence tumor growth in immune-competent C57BL/6 WT mice (Fig. 2d). Interestingly, as shown in Fig. 2e, f, overexpression of *HDAC2-AS2* strongly enhanced tumor size and tumor weight. The orthotopic model also demonstrated similar results that *HDAC2-AS2* overexpression significantly promoted tumor growth (Fig. 2g–i), together suggesting T cells may be involved in *HDAC2-AS2*-mediated tumor progression. To further investigate which immune cells were influenced by *HDAC2-AS2* overexpression, we employed flow cytometry to analyze immune components from orthotopic tumor tissues and spleen. Cytotoxic IFN-γ$^+$ and granzyme B$^+$ CD8$^+$ T cells decreased most, while immunosuppressive regulatory T cells (Treg), tumor-associated macrophages (TAM), and myeloid-derived
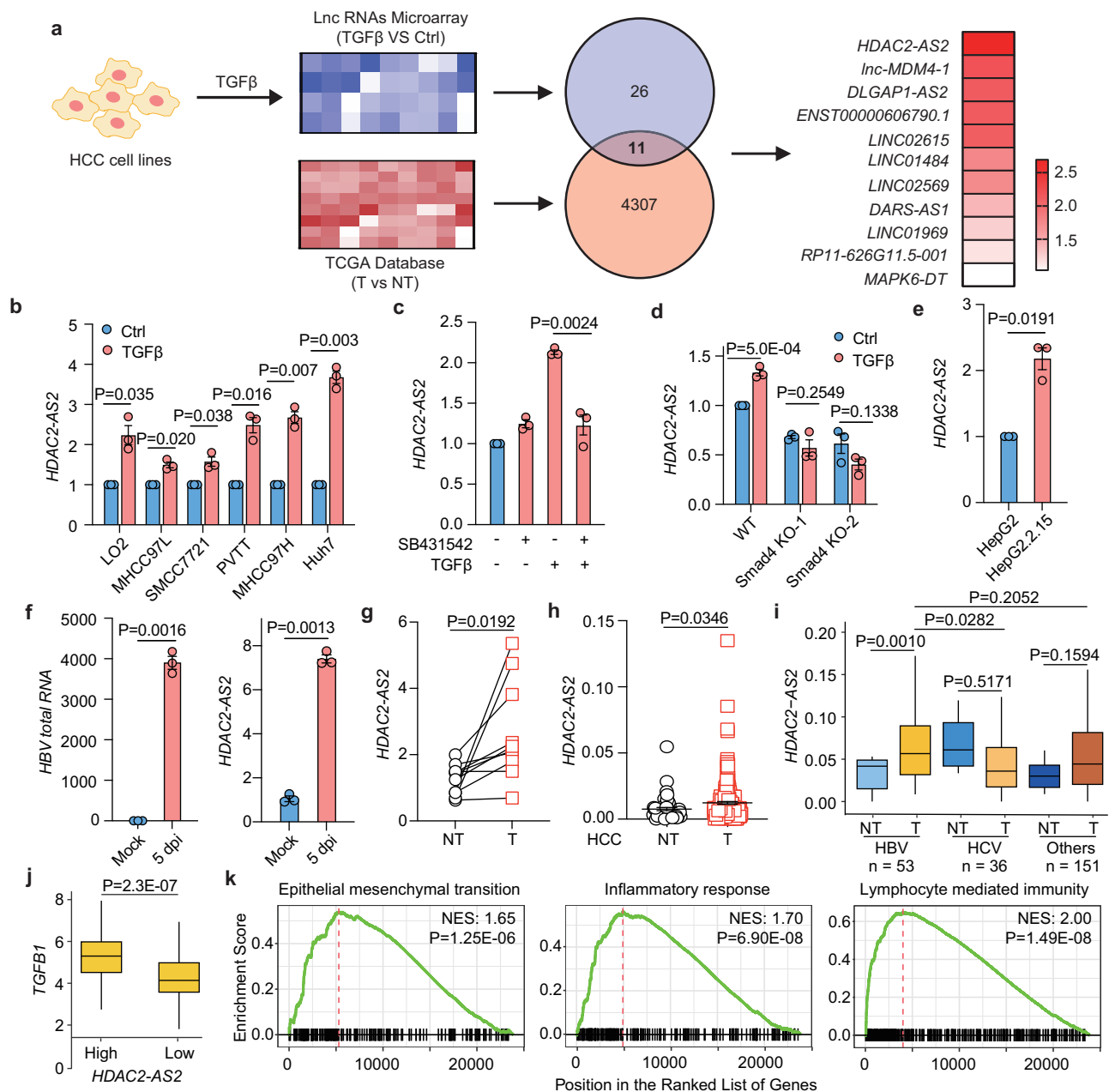
Fig. 1 | *HDAC2-AS2* was upregulated by TGFβ. a Experimental layout to identify TGFβ dependent lncRNAs. HepG2, Huh7, MHCC97, and PVTT cells were treated with TGFβ (2.5 ng/mL) for 8 h. RNA was harvested for microarray analysis of lncRNAs. Then our lncRNA microarray (TGFβ treatment vs. ctrl) merged with upregulated lncRNAs in the TCGA database (HCC samples vs. non-tumor tissues). qRT-PCR validation of indicated 11 lncRNAs relative to *β-actin* in MHCC97H cells treated with TGFβ (2.5 ng/mL) for 48 h. **b** qRT-PCR validation of *HDAC2-AS2* relative to *β-actin* in LO2, PVTT, Huh7, SMCC7721, MHCC97L, and MHCC97H cells treated with TGFβ (2.5 ng/mL) for 48 h. **c** MHCC97H cells were pretreated with 10 μM SB431542 for 1 h, followed by TGFβ treatment for 48 h. *HDAC2-AS2* expression was detected by qRT-PCR. **d** qRT-PCR analysis of *HDAC2-AS2* expression relative to *β-actin* in SMCC7721 WT and Smad4 KO cells treated with TGFβ (2.5 ng/mL) for 48 h. **e** qRT-PCR analysis of *HDAC2-AS2* relative to *β-actin* in HepG2 and HepG2.2.15 cells. **f** qRT-PCR analysis of *HDAC2-AS2* relative to *β-actin* in HepG2-NTCP cell line after HBV infection. **g** qRT-PCR analysis of *HDAC2-AS2* expression relative to *β-actin* in human HCC tissues and paired adjacent noncancerous

tissues (*n* = 10 for paired samples). **h** Elevated *HDAC2-AS2* expression in the tumor of HCC (*n* = 50, 200 for NT and T samples) in the TCGA database. **i** Boxplot showing the expression levels of *HDAC2-AS2* in tumor (T) and nontumor tissues (NT) sourced from the TCGA-LIHC database, classified according to their etiology (*n* = 53, 36, 151 for samples of HBV, HCV, and others, respectively). The boxplots denote the median with a quartile range (25–75%), and the length of whiskers represents 1.5× the IQR. **j** The expression levels of *TGFB1* in *HDAC2-AS2* low- (*n* = 157) and high- (*n* = 83) expressing tumor and nontumor tissues. The boxplots denote the median with a quartile range (25–75%), and the length of whiskers represents 1.5× the IQR. **k** GSVA analysis of epithelial-mesenchymal transition, inflammatory response, and lymphocyte-mediated immunity signatures in *HDAC2-AS2* high-expressing tumor tissues. The *P*-values were calculated based on a two-tailed permutation test. NES, normalized enrichment score. Error bars represent mean ± SEM for three independent replicates. Statistical analyses were determined by two-tailed Student's *t*-test (**b–j**). Source data are provided as a Source Data file.

suppressor cells (MDSC) were significantly increased in *HDAC2-AS2*-overexpression group, contributing to a more inhibitory TME with lower CD8/CD4 and CD8/Treg ratio. No significant changes in the frequency of immune cells within the spleen were observed between these two groups (Fig. 2j–n). These results indicate that *HDAC2-AS2* can primarily promote HCC growth by remodeling TME with more immunosuppressive Tregs, TAMs, MDSCs, and less cytotoxic CTLs.
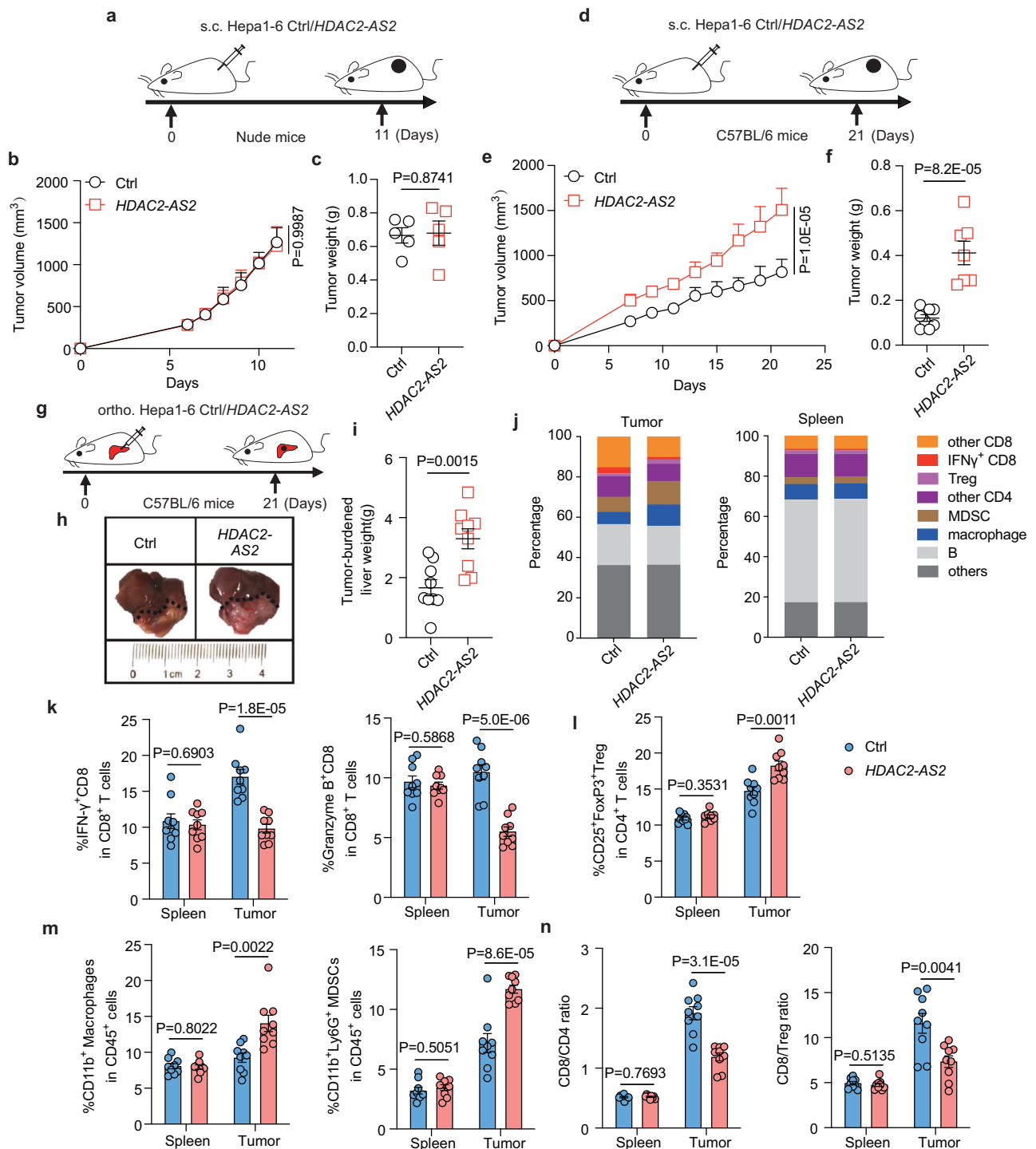
Fig. 2 | *HDAC2-AS2* promoted tumor growth in C57BL/6 mice and impaired CD8⁺ T cell function. a Experimental layout to analyze tumor growth in nude mice (**a**–**c**). Mice were subcutaneously xenografted with Hepa1-6-Ctrl or *HDAC2-AS2* cells (3 × 10⁶) for 11 days (*n* = 5 mice for each group). **b** and **c** Tumor volume (**b**) and Tumor weight (**c**) were measured (*n* = 5). **d** Experimental layout to analyze tumor growth in C57BL/6 mice. Mice were subcutaneously xenografted with Hepa1-6-Ctrl (*n* = 8) or *HDAC2-AS2* cells (*n* = 7) (1 × 10⁷) for 21 days. **e** and **f** Tumor volume (**e**) and Tumor weight (**f**) were measured in tumor-bearing C57BL/6 mice. **g** Experimental layout to analyze immune cells in C57BL/6 mice (*n* = 9 mice per group). Mice were orthotopically xenografted with Hepa1-6-Ctrl or *HDAC2-AS2* cells (3 × 10⁶) for 2 weeks. Immune cells in the tumor and spleen were harvested and analyzed. **h** and **i** Tumor weight was shown in C57BL/6 mice orthotopically xenografted with Hepa1-

6-Ctrl or *HDAC2-AS2* cells. *n* = 9 mice per group. **j** Immunophenotyping of the percentage of individual cell populations in spleen and tumor tissues by flow cytometry. **k** The percentage of IFN-γ⁺CD8⁺ T cells and Granzyme B⁺ CD8⁺ T cells in the spleen and tumor tissues was shown. *n* = 9 mice per group. **l** and **m** Flow cytometry quantification of the percentage of CD25⁺FoxP3⁺ Treg (l, gated in CD4⁺CD45⁺ cells), CD11b⁺ TAMs and CD11b⁺ Ly6G⁺ MDSCs (**m** gated in CD45⁺ cells) in spleen and tumor tissues. *n* = 9 mice per group. **n** Flow cytometry quantification of CD4/CD8 ratio and CD8/ Treg ratio in spleen and tumor tissues, gated in CD3⁺CD45⁺ cells. *n* = 9 mice per group. All error bars represent mean ± SEM. Statistical analyses were determined by two-way ANOVA (**b**, **e**) or two-tailed Student's *t*-test (**c**, **f**, **i**, **k**–**n**). Source data are provided as a Source Data file.

HDAC2-AS2 is released inside extracellular vesicles by HCC cells

Thus, we wonder how tumor-derived *HDAC2-AS2* can influence TME. Recently, tumor-derived EVs have been reported as key mediators that transfer RNAs or proteins between tumor cells and stroma in the primary tumor and distant regions[36–38], which could be a possibility for *HDAC2-AS2* to be delivered to target immune cells. To examine the presence of extracellular *HDAC2-AS2*, we extracted RNAs from the tumor culture supernatant (TCS). The levels of *HDAC2-AS2* in TCS were unchanged upon RNase A treatment but significantly decreased when treated with RNase A and Triton X-100 simultaneously (Fig. 3a), indicating that extracellular *HDAC2-AS2* was primarily membrane-associated instead of being released directly. Then, we purified EVs by differential centrifugation and further identified them by transmission electron microscopy (TEM), nanoparticle tracking analysis (NTA), western blot, and flow cytometry (Fig. 3b–e). In addition, the presence of the other 10 selected lncRNAs in Fig. 1a was undetectable, while *HDAC2-AS2* was the only lncRNA existing in EVs among the 11 candidates (Supplementary Fig. 4a, b). Besides, we purified EVs from TCS and verified that *HDAC2-AS2* was dramatically decreased when treated with RNase A and Triton X-100 simultaneously (Fig. 3f), indicating that *HDAC2-AS2* was mainly packaged in EVs. When inhibiting EVs secretion by either Rab27A knockdown or GW4869 to inhibit neutral sphingomyelinase-2 (nSMase), EV-contained *HDAC2-AS2* was reduced at the same time, while no differences were detected in cell viability and intracellular *HDAC2-AS2* levels (Fig. 3g, h and Supplementary Fig. 4c–g). These results reveal that HCC cells secreted extracellular *HDAC2-AS2* mainly in an EV-dependent manner.

Interestingly, TGFβ can upregulate the expression of EV-packaged *HDAC2-AS2* without influencing EV numbers (Fig. 3i and Supplementary Fig. 4h, i). Furthermore, when treated with TGFβ for 24 h, the genes associated with EV biogenesis and secretion were increased noticeably (Fig. 3j). We also observed higher *HDAC2-AS2* levels in EVs derived from HepG2.2.15 cells when compared with HepG2 cells, suggesting HBV may also raise EV-packaged *HDAC2-AS2* (Fig. 3k). Importantly, levels of *HDAC2-AS2* in plasma EVs, identified by TEM and WB from 9 healthy donors (HD) and 14 HCC patients, were markedly elevated in HCC patients (Fig. 3l–n), thus *HDAC2-AS2* could serve as a new biomarker for HCC diagnosis. Together, these data demonstrate that *HDAC2-AS2*, upregulated by HBV-TGFβ, can be released into EVs, thereby facilitating the HCC process.

HDAC2-AS2-containing extracellular vesicles impair CD8⁺ T cell function

To explore how EV-enclosed *HDAC2-AS2* remodeled the TME, we constructed Hepa1-6-Ctrl-EGFP-mCD63 and Hepa1-6-*HDAC2-AS2*-EGFP-mCD63 cell lines to monitor the secretion and uptake of EVs by GFP fluorescence detection (Supplementary Fig. 5a). The expression of *HDAC2-AS2* was also detected in EVs derived from these cell lines (Supplementary Fig. 5b). We first tested whether EVs can be released from Hepa1-6 cells and identified them by TEM and NTA (Supplementary Fig. 5c, d). Subsequently, we examined the uptake of GFP⁺EVs among immune components. Indeed, macrophages ingested the most EVs due to their phagocytic activity. But to our surprise, CD8⁺ T cells exhibited a higher observed EV-generated GFP⁺ signal than others, further verified by sorted tumor-infiltrated cells (Fig. 4a, b). Furthermore, we constructed another EVs-delivered system labeled with fluorescent dye DiI and incubated it with activated CD8⁺ T cells. After 24 h, CD8⁺ T cells exhibited efficient uptake of EVs determined by confocal analysis and flow cytometry (Fig. 4c, Supplementary Fig. 5e). Though there was no difference in GFP fluorescence intensity between two tumor-derived EVs, CD8⁺ T cells acquired strongly higher levels of *HDAC2-AS2* from Hepa1-6-*HDAC2-AS2*-EGFP-mCD63-derived EVs compared to the control group (Fig. 4d). Similar results were observed in human CD8⁺ T cells treated with MHCC97L-Ctrl and MHCC97L-*HDAC2-AS2* EVs (Fig. 4e).

These data indicate that EV-containing *HDAC2-AS2* can be delivered into CD8⁺ T cells.

To investigate how EV-packaged *HDAC2-AS2* influenced CD8⁺ T cell function, we evaluated the functional response of CD8⁺ T cells. As shown in Fig. 4f, g, cleaved PARP, caspase 3 protein, and apoptotic levels were increased in EVs derived from Hepa1-6-*HDAC2-AS2* cells. These findings were further confirmed in human CD8⁺ T cells (Supplementary Fig. 5f). To validate the specific role of *HDAC2-AS2*, we employed retrovirus and lentivirus systems to overexpress *HDAC2-AS2* in mouse and human CD8⁺ T cells, respectively. Increased apoptotic rates and enhanced cleaved PARP or cleaved caspase 3 protein levels were observed in both *HDAC2-AS2*-overexpressed mouse and human CD8⁺ T cells (Fig. 4h, i and Supplementary Fig. 5g, h). Consistent with these data, *HDAC2-AS2*-beared tumor-infiltrated CD8⁺ T cells exhibited higher susceptibility to apoptosis and decreased cytotoxicity (Figs. 4j and 2k). Dose dependence further established the function of EV-contained *HDAC2-AS2* in accelerating CD8⁺ T cell exhaustion with increased PD-1 expression and decreased GZMB secretion (Fig. 4k, Supplementary Fig. 5i). In contrast, *HDAC2-AS2* knockdown rescued the apoptosis and exhaustion of human CD8⁺ T cells and strengthen the activation for antitumor response, while TGFβ treatment counteracted the apoptotic effect (Fig. 4l, m, Supplementary Fig. 5j, k). Collectively, these findings indicate that tumor-derived EV-carrying *HDAC2-AS2* targets CD8⁺ T cells to impair antitumor function both in vivo and in vitro.

HDAC2-AS2 targets CDK9 to impair the function of CD8⁺ T cells

To explore the mechanism of *HDAC2-AS2* in influencing CD8⁺ T cells, we screened proteins associated with *HDAC2-AS2* in activated CD8⁺ T cells by performing RNA-pulldown assays followed by silver staining and MS. Interestingly, cyclin-dependent kinase 9 (CDK9), a key transcriptional elongation factor among the CDK family to drive oncogenesis[39,40], was identified as binding to *HDAC2-AS2*, which was further confirmed by RIP assay (Fig. 5a–c, Table S2). A series of truncated CDK9 was constructed to map the binding regions between CDK9 and *HDAC2-AS2*, demonstrating that the C-terminal of CDK9 could bind to *HDAC2-AS2* (Supplementary Fig. 6a, b). To our surprise, although CDK9 predominantly localized in the nucleus of HCC cell lines, increased expression and cytosolic localization of CDK9 in activated CD8⁺ T cells was observed (Fig. 5d, e and Supplementary Fig. 6c), consistent with previous studies that CDK9 had the intrinsic property as a nucleocytoplasmic transporter[41,42]. Both retrovirus/lentivirus-mediated *HDAC2-AS2* overexpression and EV-packaged *HDAC2-AS2* delivery in mouse and human CD8⁺ T cells promoting CDK9 degradation without affecting CDK9 mRNA expression, compared to control cells (Fig. 5f–h and Supplementary Fig. 6d–g). These results revealed that *HDAC2-AS2* could bind to cytoplasmic CDK9 in activated CD8⁺ T cells and decrease CDK9 expression.

CDK9 has been reported as the molecular target in T cell leukemia, and CDK9 inhibitors can suppress the activation of T cells[43]. Considering the different subcellular localization of CDK9 in naïve and activated CD8⁺ T cells, we evaluated the role of CDK9 in regulating CD8⁺ T cell activation and differentiation at the single-cell epigenetic level using Ti-ATAC-seq 2. This allows us to simultaneously analyze chromatin accessibility and T cell receptor (TCR) clonality in the same single T cell from our recently published dataset[44] (Fig. 5i). We then identified and annotated TCR clonality and chromatin accessibility of 4 CD4⁺ and 7 CD8⁺ T clusters from 15,022 T cells, and visualized with uniform manifold approximation and projection (Fig. 5j). Interestingly, as compared to the CD4⁺ T-cell clusters, all of the CD8⁺ T-cell clusters showed higher DNA accessibility in the *CDK9* gene locus, with highest and lowest accessibility in terminal effector-state cluster 9 (CD8-*S1PR5*-TBX21) and naïve-state cluster 4 (CD8-*GRID2*-TCF7L2) respectively, indicative of a specific role of *CDK9* DNA accessibility for CD8⁺ T cell function (Fig. 5k, l).
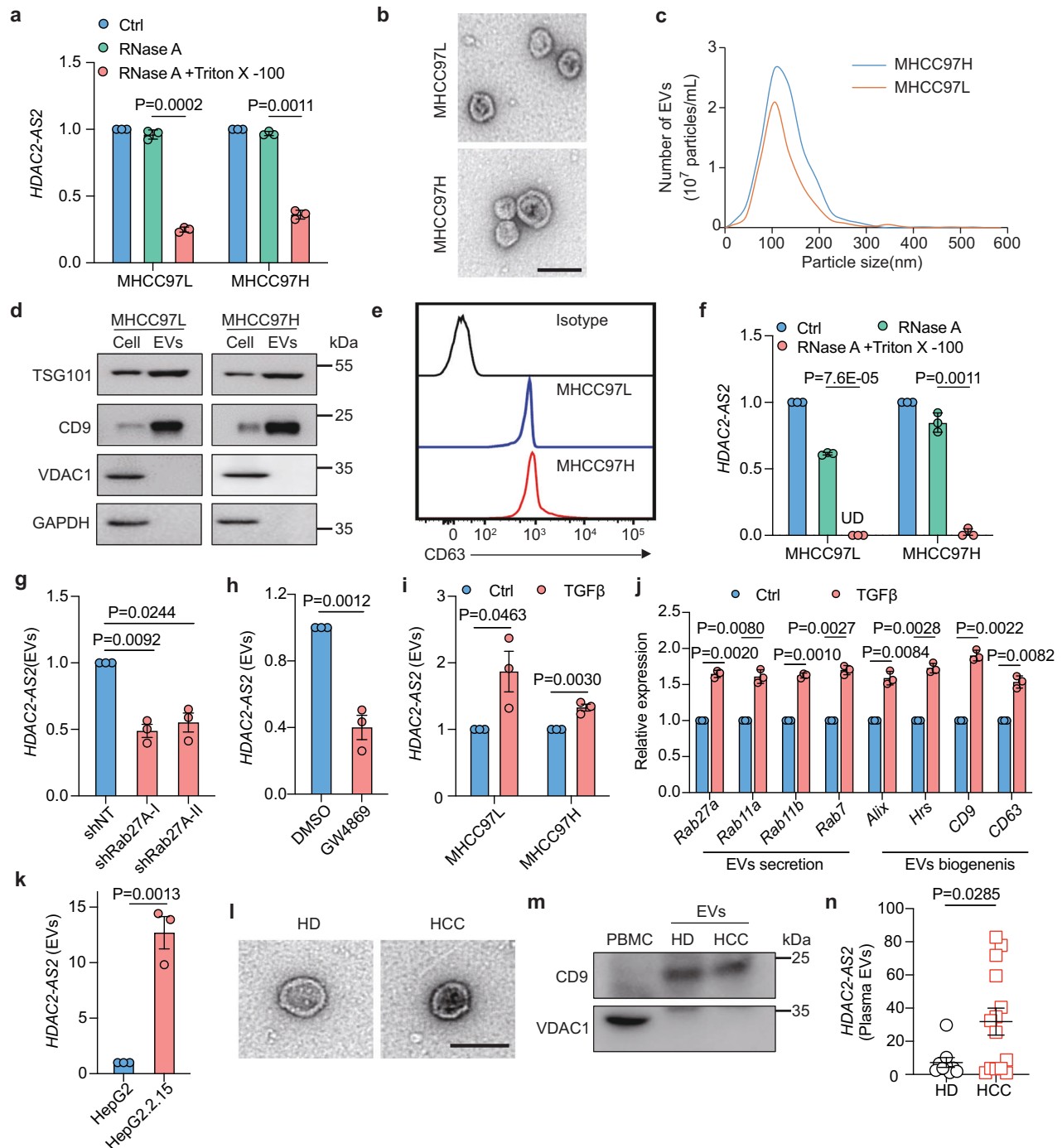
Fig. 3 | HDAC2-AS2 released inside extracellular vesicles by HCC cells. a qRT-PCR analysis of *HDAC2-AS2* expression relative to the spike-in control λ polyA⁺ RNA in the TCS of MHCC97L and MHCC97H cells treated with 2 µg/mL RNase A alone or in combination with 0.1% Triton X-100 for 20 min. **b** Representative electron microscopy images of EVs. Scale bar: 100 nm. **c** NTA analysis of EVs. **d** Immunoblotting analysis of CD9, TSG101, GAPDH and VDAC1. Representative images are shown from three independent replicates. **e** EVs were identified using CD63 antibody, Iso isotype control. **f** qRT-PCR analysis of *HDAC2-AS2* expression relative to spike-in control λ polyA⁺ RNA in the EVs from MHCC97L and MHCC97H cells treated with 2 µg/mL RNase A alone or in combination with 0.1% Triton X-100 for 20 min. UD undetectable. **g** and **h** qRT-PCR analysis of the *HDAC2-AS2* levels relative to spike-in control λ polyA⁺ RNA in the EVs derived from MHCC97H Rab27A knockdown stable cell line (**g**), or from MHCC97H after treated with 5 µM GW4869 for 48 h (**h**). **i** qRT-PCR analysis of *HDAC2-AS2* levels relative to spike-in control λ polyA⁺ RNA in the EVs of MHCC97L and MHCC97H cells that were treated with TGFβ (2.5 ng/mL) for 48 h.

j MHCC97H cells were treated with 2.5 ng/mL TGFβ for 24 h. qRT-PCR analysis was performed to assess the expression of related genes relative to *β-actin* in ctrl and TGFβ-treated cells. **k** qRT-PCR analysis of *HDAC2-AS2* expression relative to spike-in control λ polyA⁺ RNA in the EVs of HepG2 and HepG2.2.15 cells treated with RNase A (2 µg/mL) for 20 min. **l** Representative electron microscopy images of EVs isolated from plasma of healthy donors (HD, *n* = 9) and HCC patients (*n* = 14). Scale bar: 100 nm. **m** Immunoblotting analysis of CD9, VDAC1 expression in EVs isolated from plasma of HD and HCC patients. Representative images are shown from three independent replicates. **n** qRT-PCR analysis of *HDAC2-AS2* expression relative to spike-in control λ polyA⁺ RNA in the EVs isolated from plasma of HD (*n* = 9) and HCC patients (*n* = 14). EVs were purified by ultracentrifugation (**b–i**, **k–n**). Error bars represent mean ± SEM for three independent replicates. Statistical analyses were determined by two-tailed Student's *t*-test (**a**, **f–k**, **n**). Source data are provided as a Source Data file. EVs extracellular vesicles, HD healthy donors.
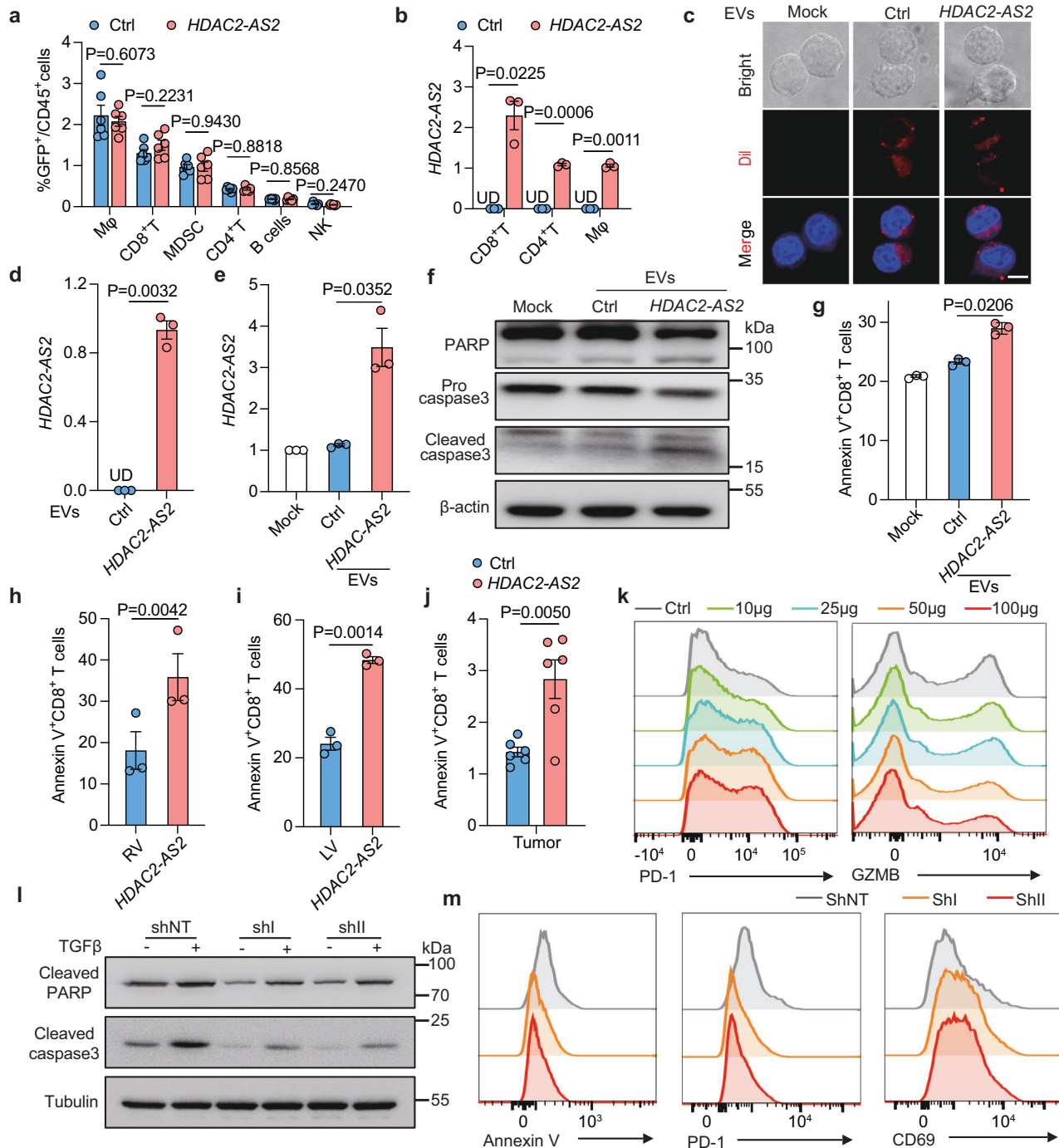
When ordering the 7 CD8+ T-cell clusters based on the *CDK9* DNA accessibility, we found the activation and cytotoxicity levels of CD8+ T-cell clusters, as indicated by gene scores of *PRF1* and *GZMK* and TF deviation scores of LEF1, EOMES, and TBX21, gradually increased along with the *CDK9* DNA openness (Fig. 5m, n). Furthermore, the analyses of TCR clonality in CD8+ T-cell clusters revealed a gradually increased clonal expansion in parallel with the *CDK9* DNA accessibility, with the highest clonal proliferation and the *CDK9* DNA accessibility observed in terminal effector-state cluster 9 (Fig. 5o), highlighting CD8+ T cell activation and cytotoxicity correlates with *CDK9* chromatin accessibility. However, we also noticed the exhaustion level increased synchronously with *CDK9* openness in cluster 2 (CD8-*TOX*-NFATC2) (Fig. 5m–o), suggesting a more critical role of CDK9 in regulating CD8+ T cell function.

Single-cell transcriptomic analysis highlights the enhanced cytotoxicity of CDK9+CD8+ T cells

To validate the findings in our epigenomic analysis, we conducted further differential gene expression analysis of CDK9+CD8+ T cells based on single-cell RNA-seq (scRNA-seq) data of patients with liver cancer[45]. 20 T-cell clusters from 16,462 intratumoral T cells of 37 patients were identified and characterized based on the marker gene expressions (Fig. 6a). According to the expression of *CD4*, *CD8A*, *CDK9*, we grouped these T cells into CDK9⁻CD4+, CDK9+CD4+, CDK9⁻CD8+ and CDK9+CD8+ T cells (Supplementary Fig. 7a). Differential gene analyses revealed CDK9+CD8+ T cells had enhanced expression of genes involved in activation including *IFI35*, *JUND*, and *STAT1*, cytotoxicity including *PRF1*, *GZMB*, and *GZMK*, and exhaustion including *TOX*, *TIGIT*, and *LAG3* (Fig. 6b). The top 200 upregulated genes involved in

Fig. 4 | _HDAC2-AS2_ Extracellular vesicles impaired CD8⁺ T cells function. a Flow cytometry analysis of GFP⁺ immune cells in tumors of orthotopically xenografted with Hepa1-6-Ctrl-EGFP-mCD63 or Hepa1-6-_HDAC2-AS2_-EGFP-mCD63 cells for two weeks (n = 6 mice). Mø: macrophage. **b** qRT-PCR analysis of _HDAC2-AS2_ levels in infiltrated CD8⁺ T, CD4⁺ T, and Mø in tumors orthotopically xenografted with Hepa1-6-Ctrl-EGFP-mCD63 or Hepa1-6-_HDAC2-AS2_-EGFP-mCD63 cells for two weeks. qRT-PCR results represent fold change relative to the macrophage group after normalization to _β-actin_ (three independent replicates). Mø macrophages, UD undetectable. **c** DiI-labeled EVs from Hepa1-6-Ctrl or _HDAC2-AS2_ cells were added to activated mouse CD8⁺ T cells for 24 h, then DiI signal was detected by confocal microscopy. Mock is PBS treatment. Scale bar: 5 μm. EVs were purified by ultracentrifugation. Representative images are shown from three independent replicates. **d** qRT-PCR analysis of _HDAC2-AS2_ relative to _β-actin_ in mouse CD8⁺ T cells after incubating with Ctrl and _HDAC2-AS2_ containing EVs for 24 h (three independent replicates). UD: undetectable. **e** Activated human CD8⁺ T cells were incubated with EVs derived from MHCC97L-Ctrl and MHCC97L-_HDAC2-AS2_ cells for 24 h, _HDAC2-AS2_ expression was detected by qRT-PCR and normalized to _β-actin_ (three independent replicates). **f** and **g** Activated mouse CD8⁺ T cells were treated with EVs from Hepa1-6-Ctrl or _HDAC2-AS2_ cells for 48 h. Apoptosis was detected by western blot (**f**) and flow cytometry (**g**) (three independent replicates). **h** Activated mouse CD8⁺ T cells were infected with retrovirus ctrl or retrovirus-_HDAC2-AS2_ for 48 h, and apoptosis was detected by flow cytometry (three independent replicates). **i** Activated human CD8⁺ T cells were infected with lentivirus ctrl or lentivirus-_HDAC2-AS2_ for 48 h, and apoptosis was detected by flow cytometry (three independent replicates). **j** Flow cytometry quantification of the percentage of Annexin-V⁺ CD8⁺T cells in tumor tissues from orthotopically xenografted mice (n = 6 mice). **k** Activated human CD8⁺ T cells were incubated with EVs derived from MHCC97L-Ctrl and MHCC97L-_HDAC2-AS2_ cells for 48 h, then the indicated signal was detected by flow cytometry. **l** Activated human CD8⁺ T cells were incubated with EVs derived from TGFβ treated ctrl and _HDAC2-AS2_ knockdown MHCC97H cells for 48 h. The protein levels of cleaved PARP and caspase3 were detected by western blot. EVs were purified by VEX reagent. Representative images are shown from three independent replicates. **m** Activated human CD8⁺ T cells were incubated with EVs derived from ctrl and _HDAC2-AS2_ knockdown MHCC97H cells for 48 h, then the indicated signal was detected by flow cytometry. EVs were purified by VEX reagent. Error bars represent mean ± SEM. Statistical analyses were determined by a two-tailed Student's _t_-test (**a, b, d, e, g–j**). Source data are provided as a Source Data file. Mφ macrophage.

pathways of the adaptive immune system, chromatin remodeling, epigenetic regulation of gene expression, were enriched in CDK9⁺CD8⁺ T cells as compared to CDK9⁻CD8⁺ T cells (Fig. 6c). A similar transcriptomic phenotype of the CDK9⁺CD8⁺ T cells was also observed in the analysis of another scRNA-seq dataset[46] (Supplementary Fig. 7b–d). To gain insights into the _CDK9_ expression in directing differentiation of CD8⁺ T cells, we constructed a lineage trajectory of CD8⁺ T cells based on the sequential differentiation states from the naïve state to either the cytotoxicity state or the exhaustion state and demonstrated that CDK9 was mainly expressed in the cytotoxicity branch of the trajectory compared to the exhaustion branch (Fig. 6d). Altogether, these results reveal the critical epigenetic role of CDK9 chromatin accessibility in regulating CD8⁺ T cell activation and differentiation, consistent with our observation in Fig. 5.

We next employed NVP-2, a selective ATP-competitive CDK9 inhibitor, to validate whether CDK9 could regulate CD8⁺ T cell function. Obviously, induced apoptosis, senescence, and exhaustion along with decreased proliferation and cytotoxicity were determined in CD8⁺ T cells when treated with NVP-2 (Fig. 6e–h), in line with the results observed in _HDAC2-AS2_-overexpressed CD8⁺ T cells (Supplementary Fig. 7e, f and Fig. 4k–m) and orthotopic models (Fig. 6i). Previous studies demonstrated that reduction of CDK9 was concomitant with attenuation of proliferative signaling mediated by p38 kinases, contributing to tumor growth by increasing the expression of PD-1[47,48], thus we detected the potential mechanism of how EV-contained _HDAC2-AS2_ induced the exhaustion of CD8⁺ T cells. As expected, both _HDAC2-AS2_-overexpressed EV-treatment or NVP-2 inhibition reduced the phosphorylation of p38, leading to increasing PD-1 expression (Supplementary Fig. 7g, h, Figs. 4k and 6g), indicating CDK9 inhibitors may accelerate the exhaustion of CD8⁺ T cells, which to some extent counted against the antitumor therapy. In summary, these results corroborated with the epigenome and transcriptome data together demonstrate that _HDAC2-AS2_-targeted CDK9 plays a key role in maintaining the physiological and pathological state of CD8⁺ T cells, thus providing therapeutic opportunities for HCC immunotherapy.

Immune checkpoint blockade (ICB) disrupts the _HDAC2-AS2_-CDK9 axis to empower CDK9⁺CD8⁺ T cell cytotoxicity

Taking account of the exhaustion phenotype from _HDAC2-AS2_-targeted CDK9 blockage in CD8⁺ T cells (Figs. 2l and 6g–i), we further explored the role of CDK9 expression in T cell response to ICB therapy in patients with HCC. We analyzed 25,516 tumor-infiltrating T cells from HCC patients with or without ICB therapy[45,49] (Fig. 7a, b). According to the therapy and expression of _CD4_, _CD8A_, and _CDK9_, T cells were classified into 8 subpopulations. Of note, the CDK9⁺CD8⁺ T cells from

patients with ICB therapy (CDK9⁺CD8⁺ T cell-ICB therapy) showed the highest expression of _CDK9_, along with cytotoxicity-associated genes such as _GZMK_, _IFNG_, and _GZMA_, in comparison to other T-cell populations. In contrast, CDK9⁺CD8⁺ T cell-ICB therapy group expressed lower levels of exhausted genes, including _TOX_, _TIGIT_, and _LAG3_, compared to CDK9⁺CD8⁺ T cells from patients without ICB therapy (Fig. 7c). Therefore, we speculated whether the ICB therapy can improve the _HDAC2-AS2_-mediated tumor process. To validate this hypothesis, mice were injected subcutaneously with Hepa1-6 tumor cells and then received anti-PD-1 or control IgG injection twice a week (Fig. 7d). Notably, anti-PD-1 treatment prominently weakened _HDAC2-AS2_-fostered tumor growth compared to the control group (Fig. 7e, f), indicating _HDAC2-AS2_-CDK9 axis-mediated tumor progression could benefit more from anti-PD-1treatment. Moreover, by examining the association between the expression of the _HDAC2-AS2_-CDK9 axis and the prognosis of HCC in TCGA database, we verified that elevated levels of _CDK9_ and _CD8A_, as well as elevated _CDK9_ expression coupled with low _HDAC2-AS2_ expression within the tumor, were correlated with extended disease-free survival (Fig. 7g). Altogether, these results underscore the significance of immune checkpoint blockade in disrupting the _HDAC2-AS2_-CDK9 axis to augment the cytotoxicity potential of CDK9⁺CD8⁺ T cells, ultimately benefiting patients (Fig. 7h).

Discussion

As one of the most complicated signaling pathways with various downstream members and target effects, the TGFβ signaling pathway plays vital roles in tumorigenesis and progression by exerting either tumor-promoting or tumor-suppressing effects. Although several lncRNAs regulated by TGFβ have been identified in proliferation, apoptosis, invasion, and metastasis so far[13–17,50], it has been a strenuous task to elucidate the function of lncRNAs in HCC progression. In this study, we identified that _HDAC2-AS2_ ranked highest among the eleven candidates, mediates the role of TGFβ in promoting HCC progression. In addition, another candidate, _DLGAP1-AS2_ has been characterized as an oncogenic lncRNA in glioma and HCC[51,52]. Interestingly, the increased _HDAC2-AS2_ expression was not only observed in HCC but also in STAD, KIRP, and KIRC tumor tissues compared to non-tumor tissues, suggesting the general role of _HDAC2-AS2_ in tumor development. Our results have verified the positive correlation between TGFβ activation and _HDAC2-AS2_ expression. Furthermore, both TGFβ blockade by either type I receptor inhibitor or _Smad4_ knockout and HBV infection are sufficient to disrupt _HDAC2-AS2_ expression, which implies _HDAC2-AS2_ is a direct target of the HBV-TGFβ/Smad pathway.

The paradoxical results obtained from the different phenotypes of _HDAC2-AS2_ overexpressing tumor cells in nude mice and
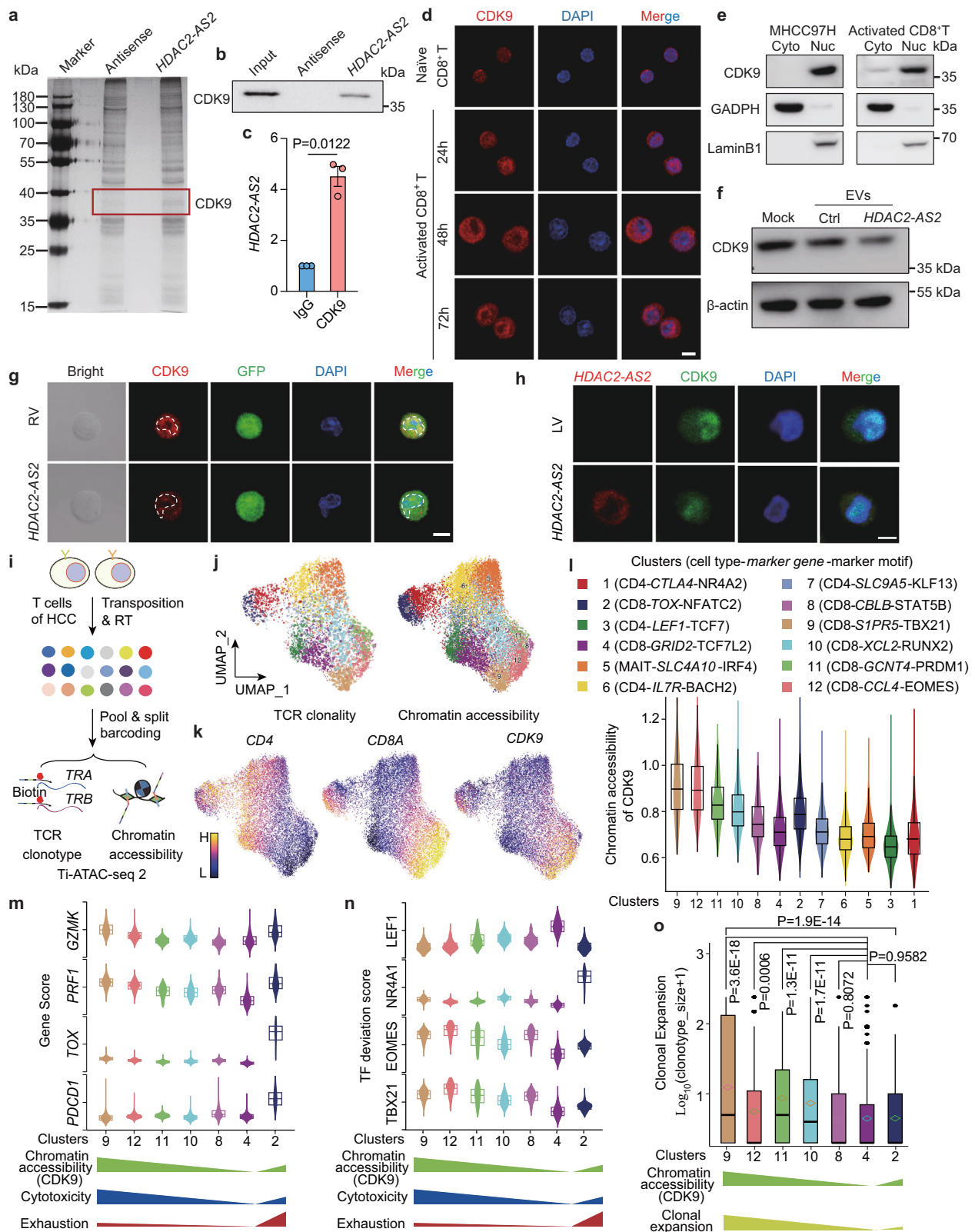
immune-competent C57BL/6 mice provided evidence that *HDAC2-AS2* plays a crucial role in modulating TME. The overexpression of *HDAC2-AS2* selectively resulted in the loss of CD8⁺ T cells, enhanced features of exhaustion, and decreased production of cytokines in tumor tissues, while immunosuppressive Tregs, TAMs, MDSCs were accumulated in TME, suggesting the potential unexplored dual effects of *HDAC2-AS2* on facilitating pro-tumor immunosuppression and antitumor inhibition

simultaneously. Accumulating evidence has shown that EVs can, in vitro, impair differentiation and maturation of dendritic cell[53], affect proliferation, activation, and apoptosis of CD4⁺ and CD8⁺ T lymphocytes[54–56], decrease the cytotoxicity of natural killer cells and macrophages[57], and promote the differentiation of immunosuppressive cells such as Tregs[58] or myeloid cells[59]. Specifically, EVs containing protein and noncoding RNAs could educate immune cells, which are

Fig. 5 | *HDAC2-AS2* targeted CDK9 to impair the function of CD8^{+} T cells. a Silver staining of the SDS-PAGE gel containing aliquots of samples derived from proteins pulled down by *HDAC2-AS2* (right lane) or its antisense RNA (left lane) in mouse CD8^{+} T cells. The arrows indicate the gels submitted for mass-spectrometry, identifying CDK9 as the band unique to *HDAC2-AS2*. Representative images are shown from three independent replicates. **b** Western blot analysis of the interaction of CDK9 with *HDAC2-AS2* (treated the same as panel **a**). Representative images are shown from three independent replicates. **c** RIP analysis of the interaction between CDK9 and *HDAC2-AS2* (three independent replicates). **d** The expression of CDK9 in naïve and activated mouse CD8^{+} T cells (24, 48, 72 h) was detected by confocal microscopy. Scale bar: 5 μm. Representative images are shown from three independent replicates. **e** Western blot analysis of CDK9 expression in nuclear and cytoplasmic fractions of activated mouse CD8^{+} T cells and MHCC97H cells. Representative images are shown from three independent replicates. **f** Activated mouse CD8^{+} T cells were treated with EVs from Hepa1-6-Ctrl or *HDAC2-AS2* cells for 48 h, mock is PBS treatment. CDK9 expression was detected by western blotting. EVs were purified by ultracentrifugation. Representative images are shown from three independent replicates. **g** The expression of CDK9 in activated mouse CD8^{+} T cells of retrovirus ctrl and retrovirus-*HDAC2-AS2* infection was observed by confocal microscopy. Scale bar: 5 μm. Representative images are shown from three independent replicates. **h** FISH assay showing the localization of *HDAC2-AS2* and

CDK9 in activated human CD8^{+} T cells of lentivirus ctrl and lentivirus-*HDAC2-AS2* infection. Scale bar: 5 μm. Representative images are shown from three independent replicates. **i** Experimental layout for single-cell Ti-ATAC-seq 2 to analyze chromatin accessibility and T cell receptor (TCR) clonality. **j** The UMAP projection displays T cells from HCC patients, illustrating the landscape of TCR clonality (left; indicated by the sizes of TCR clonotypes) and chromatin accessibility (right) from Ti-ATAC-seq 2 datasets. Each color represents a T-cell cluster. **k** The chromatin accessibility, indicated by gene scores of the indicated genes, is overlaid on the UMAP embedding. **l** Violin plot showing the chromatin accessibility as indicated by gene scores of CDK9 of the T-cell clusters. Each color represents a T-cell cluster, the cells of each cluster were obtained from patients ($n = 9$). **m–o** Violin plots showing the gene scores of indicated genes (**m**) and ChromVAR TF-motif bias-corrected deviation scores of indicated TF regulators (**n**) across the CD8 T-cell clusters. The cytotoxicity of the cluster is indicated by the gene scores of GZMK and PRF1, whereas the exhaustion of the cluster is indicated by the gene scores of TOX and PDCD1. (**o**). Boxplot showing the T-cell clonal expansion as indicated by the log10 (clonotype size +1) across the CD8 T-cell clusters. The boxplots denote the median with a quartile range (25–75%), and the length of whiskers represents 1.5x the IQR. The cells of each cluster were obtained from patients ($n = 9$). Statistical analyses were determined by a two-tailed Student's *t*-test (**c**, **o**). Source data are provided as a Source Data file. Cyto cytoplasmic, Nuc nuclear, RV retrovirus.

---

critical for the establishment of the pre-metastatic niche[36,38]. In the present study, we observed that *HDAC2-AS2* was packaged in tumor-derived EVs. Not only *HDAC2-AS2* but also EV-related gene expressions were increased after TGFβ treatment or HBV infection. These results suggest that HBV-TGFβ might contribute to EV biogenesis and secretion. However, the number of EVs did not increase after TGFβ treatment, indicating the complexity of EVs released regulation following TGFβ treatment. Last but not least, we observed higher *HDAC2-AS2* expression in EVs isolated from the plasma of HBV-associated HCC patients, indicating its potential as a new biomarker for HCC.

In vitro incubation with DiI-labeled EVs suggested CD8^{+} T cells can uptake EVs, which to some extent, implied the internalization of EVs into tumor-infiltrated CD8^{+} T cells in TME in a similar manner. Due to the limitations of lipid dye staining in EVs[60–62], a more reliable method was established. EVs derived from Hepa1-6-Ctrl/*HDAC2-AS2*-EGFP-mCD63 cells were acquired through ultracentrifugation. The presence of green fluorescence of EV-GFP in CD8^{+} T cells further confirmed the uptake of EVs by CD8^{+} T cells both in vitro and in vivo. Both EV treatment and retrovirus-mediated *HDAC2-AS2* overexpression induced the reduction of IFN-γ expression and apoptosis of CD8^{+} T cells. In addition, given the vital roles of immunosuppressive cytokines such as IL-10 and TGFβ, as well as inflammatory cytokines such as type I interferons (IFNs) and IL-6, in regulating CD8^{+} T cells function[63], whether these cytokines are also involved in extracellular *HDAC2-AS2* impaired CD8^{+} T cells function requires further investigation.

Interestingly, *HDAC2-AS2* interacts with CDK9, a key transcriptional elongation factor that can shuttle between the nucleus and cytoplasm[41,64,65]. This interaction reminds us of the subcellular translocation of CDK9. We indeed observed higher expression and more cytosolic location of CDK9 in activated CD8^{+} T cells, whereas in tumor cells, CDK9 mainly localizes in the nucleus. This different localization pattern could explain why *HDAC2-AS2* does not affect the tumor process itself but impairs the antitumor response of CD8^{+} T cells. More importantly, both *HDAC2-AS2* overexpression and treatment with *HDAC2-AS2* cell-derived EVs can decrease CDK9 expression in CD8^{+} T cells. Epigenome and transcriptome data indicate that CDK9 is strongly correlated with activation and cytotoxicity of CD8^{+} T cells, while exhausted CD8^{+} T cells showed a moderate expression of CDK9. Therefore, inhibition of CDK9 by NVP-2 leads to apoptosis, senescence, and exhaustion, along with decreased proliferation and cytotoxicity in CD8^{+} T cells. This phenotype is similar to that observed in *HDAC2-AS2*-overexpressed CD8^{+} T cells and orthotopic models, resulting in tumor progression and metastasis. However, this finding somehow contradicts previous studies, which suggest CDK9 is a novel

target for anticancer therapeutics, and multiple inhibitors are currently in clinical trials for advanced malignancies[39,66]. Nevertheless, several phase I/II studies have shown no objective tumor responses or efficacy superior to chemotherapeutics in colorectal, ovarian, pancreatic, lung, and breast cancers[67–70]. A possible explanation is that, although CDK9 inhibitors can reduce tumor growth, they simultaneously induce exhausted CD8^{+} T cells, which, to some extent, weakens the antitumor effect. Besides, we noticed that *HDAC2-AS2* can also interact with IMP4, SLP2, AURKB, and STRAP, which have been established to promote tumorigenesis (Table S2), suggesting the potential multiple effects of *HDAC2-AS2*.

To avoid this "side-effect", combination therapy could be a better choice for implementing a precise strategy. Notably, anti-PD-1 treatment prominently weakened *HDAC2-AS2*-fostered tumor growth, indicating tumor progression mediated by the *HDAC2-AS2*-CDK9 axis is more sensitive to ICB, thus providing therapeutic opportunities for HCC immunotherapy. Collectively, our findings have significant implications for expanding our understanding of lncRNAs in HCC pathogenesis, which modulated immune cells to create a favorable TME, suggesting the *HDAC2-AS2*-CDK9 axis could serve as a new evaluable biomarker for HCC precision therapy.

Methods

Ethical statement

This study was approved by the Ethics Committee of the Institute of Biophysics, Chinese Academy of Sciences. All animal care, experiments, and study protocols were approved by the Animal Care and Use Committee of the Institute of Biophysics, Chinese Academy of Sciences. The maximal tumor size did not exceed the maximum tumor size of 2 cubic centimeters for tumor models. All clinical samples were collected with written informed consent from patients, and ethical approval was granted from the committees for ethical review at Second Military Medical University.

Cell lines and reagents

HEK293T and Hepa1-6 cell lines were purchased from ATCC. The human hepatoma cell lines HepG2, HepG2.2.15, PVTT, Huh7, SMCC7721, MHCC97L, MHCC97H, and HCCLM9 were obtained from the Cell Bank of Shanghai Institute of Cell Biology, Chinese Academy of Sciences. HepG2-hNTCP cell line was a gift from the National Institute of Biological Sciences, Beijing, China (Dr. Wenhui Li). All these cells were maintained in high glucose DMEM (Gibco) supplemented with 10% FBS (Hyclone), 100 μg/mL penicillin, and 100 U/mL streptomycin. These cells were incubated at 37 °C in a humidified atmosphere of 5%
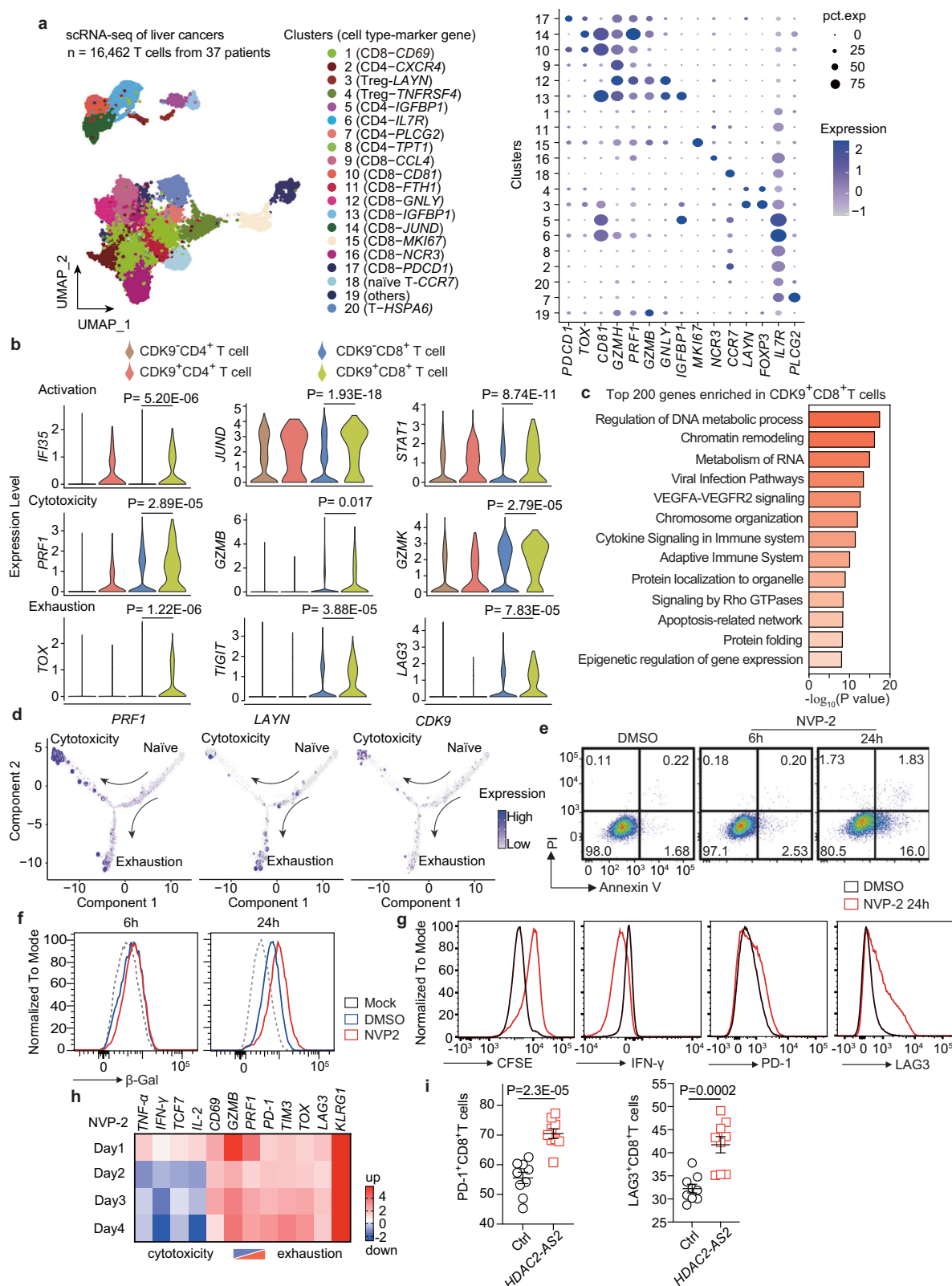
CO_2. Recombinant human TGFβ1 was purchased from Peprotech (Peprotech Inc., USA) and used at a concentration of 2.5 ng/mL. GW4869 was purchased from Sigma Aldrich.

Animal model

5–6 weeks old male athymic BALB/c nu/nu SPF mice (Cat. 401#) and C57BL/6 wildtype SPF mice (Cat. 213#) were purchased from the Beijing Vital River Laboratory Animal Technology Co., Ltd (Beijing, China) and all the mice were co-housed in the animal breeding facility affiliated with the Institute of Biophysics, Chinese Academy of Sciences, under specific pathogen-free conditions with a maximum occupancy of 5 mice per cage. For the subcutaneous injection model, 5×10^6 Hepa1-6-Ctrl or Hepa1-6-*HDAC2-AS2* cells resuspended in 0.1 mL PBS were subcutaneously implanted into the right flank of nude mice

Fig. 6 | Single-cell transcriptomic analysis highlighted the enhanced cytotoxicity of CDK9⁺CD8⁺ T cells. a Left: The scRNA-seq (GEO: GSE151530) UMAP projection of the 16,462 T cells from 37 patients with liver cancer. Each color represents a T-cell cluster. Cell types and marker genes are assigned to each cluster. Right: Expression levels of marker genes identified for clusters. **b** Violin plot showing the expression profiles of genes related to T-cell activation (top), cytotoxicity (middle), and exhaustion (bottom). A Wilcoxon Rank Sum test was performed to determine the P values (two-tailed test). **c** Pathway enrichment of top 200 marker genes enriched in CDK9⁺CD8⁺ T cells as compared to CDK9⁻CD8⁺ T cells using Metascape analysis. Significance shown by the Bonferroni-corrected P values (two-tailed test). **d** The gene expression of *PRF1*, *LAYN*, *CDK9* overlaid on the cell trajectory projection. The size and color represent the gene expression levels. **e** Activated mouse CD8⁺ T cells were treated with 250 nM NVP-2 for 6 h or 24 h, and

apoptotic cells were detected by flow cytometry. **f** Activated mouse CD8⁺ T cells were treated with 250 nM NVP-2 for 6 h or 24 h, and senescent cells were detected by flow cytometry. β-Gal positive cells are shown as senescent cells. **g** Activated mouse CD8⁺ T cells were treated with 250 nM NVP-2 for 24 h, and then the indicated signal was detected by flow cytometry. **h** Activated mouse CD8⁺ T cells were treated with 100 nM NVP-2 for indicated days, then the cytotoxicity- and exhaustion-related genes were determined by qRT-PCR. The heat map showed the fold changes when compared to the DMSO group each day. **i** Flow cytometry quantification of the percentage of PD-1⁺CD8⁺T and LAG3⁺ CD8⁺T in tumor tissues from orthotopically xenografted mice (*n* = 9 for each group). Error bars represent mean ± SEM. Statistical analyses were determined by a two-tailed Student's *t*-test. Source data are provided as a Source Data file.

and C57BL/6 mice for indicated days. For the liver orthotopic injection model, C57BL/6 mice were orthotopically injected with a mixture containing matrigel and Hepa1-6-Ctrl or *HDAC2-AS2* cells (3×10^6) for three weeks. The treated mice were promptly euthanized with CO_2 gas at the endpoints of the experiments. Tumor weight was measured, and immune cells in the spleen and tumor tissues were harvested and analyzed by flow cytometry.

Patients

The detailed clinical characteristics of these patients are listed in Table S3.

Rapid amplification of cDNA ends

5′ and 3′ RACE was conducted using the SMARTer® RACE cDNA Amplification Kit (Clontech, Palo Alto, CA) according to the manufacturer's instructions. RACE PCR products were separated by agarose gel electrophoresis, cloned into pEASY-Blunt vectors (Transgen, China), and sequenced. The gene-specific primers used for the RACE analysis of *HDAC2-AS2* are as follows: 3′RACE: CCTGGGGGTGACGA-CAACCACTGAA, 5′RACE: CATCGCCCCAGTGCCTGATTGGCATCC.

Plasmid construct and cell transfection

The cDNA of *HDAC2-AS2* was amplified using I-5™ High-Fidelity DNA Polymerase (China) and subsequently subcloned into the PCDH-CMV-MCS-EF1-puromycin lentiviral vector. HA-tagged truncated fragments of mouse CDK9, corresponding to amino acids 1-195 (N-terminal), 150-372 (C-terminal), and the full-length CDK9, were cloned into pCDNA3.1 (+) plasmid. The full-length cDNA of mouse CD63 was subcloned into the pEGFP-C1 vector to generate an N-terminal GFP fusion protein, termed EGFP-CD63, which was then subcloned into the PCDH-CMV-MCS-EF1-hygromycin lentiviral vector. Moreover, shRNA oligos were synthesized by Sangon Co. Ltd., and double-strand oligos were inserted into the lentiviral pLKO.1-hygromycin vector (Addgene) after annealing. Oligonucleotides encoding single guide RNAs (sgRNAs) to delete *Smad4* were cloned into the lentiCRISPRv2 vector (Addgene, #52961). The sequences used for shRNA and sgRNA are listed in Table S4. To produce lentivirus, HEK293T cells were co-transfected with the lentiviral vector described above and packaging vectors psPAX2 and pMD2.G using Lipofectamine 2000 (Invitrogen, USA). Culture supernatants were collected at 48 and 72 h post-infection. To generate Smad4-deficient SMCC7721 cells and Hepa1-6 Ctrl/*HDAC2-AS2* overexpression cells, cells were infected with lentivirus together with polybrene (8 μg/mL) using the spin infection method. Cells were selected with puromycin (1 μg/mL) for ten days. To generate Hepa1-6 Ctrl/*HDAC2-AS2*-EGFP-CD63 cells, stable Hepa1-6 Ctrl/*HDAC2-AS2* cells were further infected with PCDH-EGFP-CD63-hygromycin lentivirus and selected with hygromycin (100 μg/mL) for two weeks.

Furthermore, *HDAC2-AS2* was subcloned into the pMX-IRES-GFP retroviral vector and pCDH-GFP lentiviral vector to generate pMX-*HDAC2-AS2*-IRES-GFP and pCDH-*HDAC2-AS2*-GFP plasmids, respectively. Plat-E packaging cells were transfected with Lipofectamine

2000 and then cultured for 48-72 hours. The medium containing retrovirus was collected and centrifuged at 25,000×*g* for 2 h and stored at −80 °C until T cell infection. For human and mouse CD8⁺ T cell infection, naïve CD8⁺ T cells were sorted by BD Aria III cell sorter. After 24 h of activation, T cells were infected with pre-enriched retrovirus or lentivirus and 8 μg/mL polybrene (Sigma Aldrich) by centrifuging at 800×*g* for 1.5 h at 25 °C. After infection, the cells were replaced with fresh medium and harvested for intracellular staining, flow cytometry apoptosis detection, qRT-PCR, and western blot analysis.

RNA extraction and qRT-PCR

Total RNAs (HCC cell lines, HCC clinical samples, and extracellular vesicles) were extracted using Trizol (Invitrogen, USA) following the manufacturer's protocols. Total RNA in culture medium was extracted from fixed volume (350 μL) by mirVana PARIS Kit (Ambion, USA). Reverse transcription reaction was performed using the Reverse Transcription Master Kit (Takara). Quantitative real-time PCR was conducted on triplicate samples in a reaction mix containing SYBR Premix Ex TaqII (Takara) using the ViiA 7 Real-Time PCR system (Applied Biosystems, USA). The mRNA and lncRNA levels were normalized to *β-actin* in cell and tissue samples. *HDAC2-AS2* expressions in plasma and MHCC97H and MHCC97L cells derived medium and EVs (2×10^{10} particles) were normalized to a synthesized exogenous reference λ polyA⁺ RNA (Takara). The primer sequences used for qRT-PCR are listed in Table S5.

RNA-pull down assay

RNA pulldown assay was performed as described previously[71]. Briefly, specific primers containing the T7 promoter and *HDAC2-AS2* sequences were designed. PCDH- *HDAC2-AS2* plasmids were used as templates to add the T7 promoter to the sense and antisense ends of *HDAC2-AS2* by PCR amplification. Then biotin-labeled *HDAC2-AS2* transcripts and their antisense were obtained using in vitro transcription with T7 RNA polymerase and Biotin RNA Labeling Mix (Roche), treated with RNase-free DNase I (Promega) for 10 min and purified with RNeasy Mini Kit (QIAGEN). 3 μg biotinylated RNA was heated to 90 °C for 2 min, put on ice for 5 min, supplied with RNA structure buffer (10 mM Tris pH 7, 0.1 M KCl, 10 mM MgCl₂), and then shifted to room temperature (RT) for 25 min to allow proper secondary structure formation. Followed by a 6 h incubation at 4 °C with activated CD8⁺ T cell lysates. Then streptavidin-conjugated agarose beads (Invitrogen) were added to each binding reaction and further incubated at 4 °C overnight. The beads were washed five times and boiled in SDS buffer, followed by western blot detection and silver staining. Differential bands were excised for mass spectrometry (LTQ Orbitrap XL) analysis.

RNA immunoprecipitation

RIP assay was carried out as described previously[71]. The cells were washed with cold PBS three times and irradiated at 150 mJ/cm² at 254 nm in a UV crosslinker. Cells were collected and lysed in 1 mL RIP
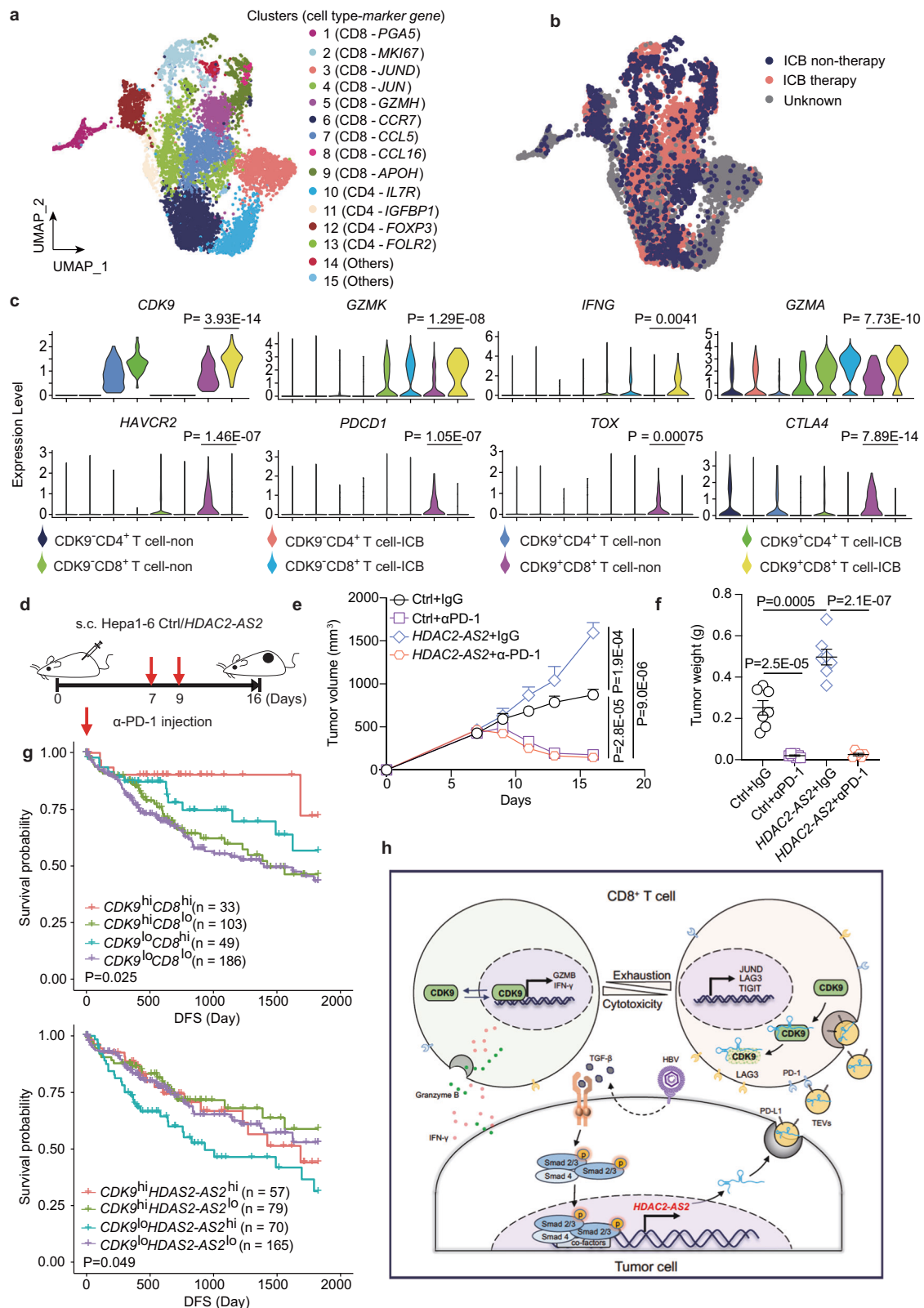
buffer (50 mM Tris–HCl pH7.5, 150 mM NaCl, 1% NP-40, 0.5% sodium deoxycholate, 1 mM PMSF, 2 mM VRC, protease inhibitor cocktail) for 30 min on ice. The lysates were pre-cleaned using 15 µL Dynabeads protein G (Invitrogen) with 20 µg/mL yeast tRNA for 1 h at 4 °C. Then the pre-cleaned lysates were further incubated with Dynabeads G that were pre-coated with 2 µg antibodies for CDK9 or IgG for 6 h at 4 °C. The beads were washed 3 × 5 min with wash buffer I (50 mM Tris–HCl

pH7.5, 1 M NaCl, 1% NP-40, 1% sodium deoxycholate, 2 mM VRC) and 3 × 5 min with wash buffer II (50 mM Tris–HCl pH7.5, 1 M NaCl, 1% NP-40, 1% sodium deoxycholate, 2 mM RVC, 1 M urea). Followed by eluting immunoprecipitated complex by adding 140 µL elution buffer (100 mM Tris–HCl pH7.0, 5 mM EDTA, 10 mM DTT, 1% SDS), 40 µL was used for western blotting analysis and 100 µL for RNA extraction. 5 µL 10 mg/mL proteinase K was added to the RNA sample and incubated at

Fig. 7 | Immune checkpoint blockade (ICB) disrupted the *HDAC2-AS2*-CDK9 axis to empower CDK9⁺ CD8⁺ T cell cytotoxicity. a The scRNA-seq (GEO: GSE151530 and GSE149614) UMAP projection of the tumor-infiltrating T cells from patients with liver cancer. Each color represents a T-cell cluster. Cell types and marker genes are assigned to each cluster. **b** UMAP plot showing the information of patients with or without immune checkpoint blockade (ICB) therapy. **c** Violin plot showing the expression profiles of indicated genes. These T-cell groups were grouped based on the ICB therapy and expression of *CD4*, *CD8A*, and *CDK9* in each cell. A Wilcoxon Rank Sum test was performed to determine the *P* values (two-tailed test). **d** Experimental layout to analyze the effect of anti-PD-1treatment in inhibiting

tumor growth in C57BL/6 WT mice (*n* = 7 mice). Mice were subcutaneously xenografted with Hepa1-6-Ctrl or *HDAC2-AS2* cells (1 × 10⁷) for 16 days and received anti-PD-1 treatment at day 7 and day 9. **e** and **f** Tumor volumes (**e**) and Tumor weight (**f**) are shown in C57BL/6 WT mice subcutaneously xenografted with Hepa1-6-Ctrl or *HDAC2-AS2* cells and received anti-PD-1 treatment. *n* = 7. **g** The disease-free survival curve based on the TCGA HCC data showing patients with higher expression of *CDK9* and *CD8A*, or *CDK9* and *HDAC2-AS2* in tumor had better prognosis. Log-rank test was performed to determine the *P* values. **h** Working model. Error bars represent mean ± SEM. Statistical analyses were determined by two-way ANOVA (**e**) or two-tailed Student's *t*-test (**f**). Source data are provided as a Source Data file.

55 °C for 40 min, then RNA was extracted, digested with DNase I (Ambion) for 10 min at 37 °C and used for cDNA synthesis, followed by qRT-PCR analysis.

Western blot

The cells were harvested, washed with cold PBS, and lysed in RIPA buffer supplemented with protease inhibitor cocktail and phosphatase inhibitor on ice for 30 min. Then the lysates were centrifuged at 20,000×*g* for 10 min at 4 °C. The protein concentration was measured using the Pierce BCA protein assay kit (Thermo Scientific). Equivalent amounts of protein (20 μg) from each sample were loaded and separated by SDS–PAGE gels and transferred to PVDF membranes. After blocking with 5% nonfat milk for 1 h at room temperature, then the membranes were incubated with specific primary antibodies at 4 °C overnight. The membranes were washed three times with TBST, and incubated with HRP-conjugated secondary antibodies for 1 h at room temperature. Followed by washing with TBST three times, and then the membranes were detected by chemiluminescence using an HRP substrate (Millipore).

Immunofluorescence staining

Naïve and activated CD8⁺ T, along with MHCC97H cells, were fixed with 4% PFA for 20 min and permeabilized in 0.5% Triton X-100 supplied with 1% BSA for 30 min at room temperature, then the cells were incubated with primary specific antibodies at 4 °C overnight. The cells were incubated with appropriate fluorescence-conjugated secondary antibodies for 1 h at room temperature after washing with PBS three times. Subsequently, the cells were stained with DAPI for 5 min. Followed by detection with the Zeiss LSM700 laser-scanning confocal microscope.

Extracellular vesicle purification and characterization

Extracellular vesicles from cell culture and human serum were purified and characterized according to MISEV 2018 guidelines. Extracellular-vesicles-depleted FBS was acquired after ultracentrifugation at 100,000×*g* for 24 h. Cells were cultured with extracellular-vesicles-depleted FBS for 48 h, then extracellular vesicles were obtained by following standard centrifugation steps as previously described[72]. Briefly, debris and dead cells in the medium were removed by centrifugation at 300×*g* for 10 min, followed by further centrifugation at 2000×*g* for 10 min. The supernatant was then centrifuged at 10,000×*g* for 30 min and then filtrated through a 0.22 μm filter at room temperature. The supernatant was then subjected to ultracentrifugation at 100,000×*g* for 18 h at 4 °C. After washing with PBS (100,000×*g* for 18 h), the pellet containing extracellular vesicles was resuspended in PBS and stored at −80 °C. In addition, 5 mL of human plasma from healthy donors and HCC patients was diluted with PBS (1:2) and centrifuged at 1000×*g* for 10 min and 10,000×*g* for 1 h at 4 °C, followed by filtration through a 0.22 μm filter. 6 mL of 20% sucrose was slowly added to the bottom of the supernatant and plasma to form a sucrose cushion to maintain the morphology and integrity of the extracellular vesicles. The ultracentrifugation and storage were described above. Besides, the

VEX Exosome Isolation Reagent (Vazyme, Cat#R601) was also used for extracellular vesicle purification. 2 mL reagent was added into 6 mL filtrated supernatant to form the mixtures, which were subsequently incubated at 4 °C for up to 16 h and then centrifuged 10,000×*g* for 30 min at 4 °C. The extracellular vesicles were resuspended in PBS and stored at −80 °C.

The characterization of extracellular vesicles was examined by transmission electron microscopy using negative staining. The markers CD9 and TSG101 of extracellular vesicles were detected by western blotting. Furthermore, pre-enriched EVs obtained by ultracentrifugation were treated according to the protocols of the EV-human CD63 isolation/detection kit (Invitrogen, Cat#10606D). Briefly, pre-enriched EVs (100 μL) were mixed with 20 μL dynabeads coated with anti-human CD63 antibody overnight at 4 °C, then bead-bound EVs were isolated using a magnetic separator. Subsequently, the beads-bound EVs were washed and stained with PE mouse anti-human CD63 antibody (BD Biosciences, Cat#561925). In addition, 20 μL dynabeads were stained with PE Mouse IgG1, κ isotype control antibody (BD Biosciences, Cat#555749). PE signals of beads were analyzed by flow cytometry.

Transmission electron microscopy (TEM)

EVs were fixed with 4% paraformaldehyde (PFA; Sigma Aldrich) (1:1) and loaded onto a TEM copper grid and then washed with PBS, 1% glutaraldehyde, and distilled water. EVs were then incubated with 4% uranyl acetate and visualized under a Tecnai Spirit transmission electron microscope (FEI/Phillips, USA) at 100 kV.

Nanoparticle tracking analysis

Numbers and sizes of EVs were evaluated using a NanoSight N300 system (Malvern Instruments, Malvern, UK). The samples were monitored with the use of a 488 nm laser and a digital camera. In brief, the EV samples derived from equal numbers (5 × 10⁶) of MHCC97L, MHCC97H, and Hepa1-6 cells were diluted with PBS (200×). 2 mL of EVs were separated using a needle and syringe, and simultaneously injected into the NanoSight sample cubicle, and 30 s motion videos were captured per measurement. The camera level and detection threshold were set at values of 16 and 7, respectively. NanoSight NTA3.2 software was used for data analysis. For each sample, measurement was independently performed three times. EV concentration was calculated as the average concentration of the three times.

In vitro extracellular vesicle treatment

For in vitro EVs treatment, a total of 2.5 × 10⁸ EVs (equivalent to those collected from 6 × 10⁶ producer cells, 50 mL culture medium) derived from Hepa1-6-Ctrl or Hepa1-6-*HDAC2-AS2* cells were added to 2 × 10⁵ activated CD8⁺ T cells for 48 h, PBS as a control treatment. Then, the cells were collected for western blot analysis, RNA extraction, and flow cytometry detection. For in vitro EVs labeling, DiI (Beyotime Biotechnology, China) was added to PBS buffer or EVs suspension at a concentration of 1 μM and incubated for 30 min at 37 °C, followed by washing through exosome spin columns (MW3000) (Invitrogen) to

remove excess dye. DiI-labeled EVs were incubated with activated CD8⁺ T cells for 24 h. As a control, PBS buffer containing free DiI dye was washed through exosome spin columns. In addition, a total of 2×10^8 EVs (equivalent to those collected from 5×10^6 producer cells in 50 mL of culture medium) derived from Hepa1-6-Ctrl-EGFP-mCD63 or Hepa1-6-*HDAC2-AS2*-EGFP-mCD63 cells were added to 2×10^5 activated CD8⁺ T cells and incubated for 24 h.

Flow cytometry
Single-cell suspensions were generated from mouse tumors, spleen, and lymph nodes, as indicated. Lymphocytes were obtained from the lymph nodes of C57BL/6 mice, and naïve CD8⁺ T cells (CD4⁻CD8⁺CD62L⁺CD44⁻CD25⁻) were sorted by BD Aria III cell sorter after staining with specific antibodies. Naive mouse T cells were activated with 2 μg/mL anti-CD3 and 1 μg/mL anti-CD28 (Biolegend). Human peripheral blood (hPBMC) naïve CD8⁺ T cells were purified by staining with specific antibodies (CD8⁺CD4⁻CD45RA⁺CD25⁻) and stimulated with 2 μg/mL anti-human CD3 and 1 μg/ml anti-human CD28 (Biolegend) for 2 days. Cells were cultured in R10 complete medium (RPMI1640, 10% FBS, 1% penicilin–streptomycin, 25 mM HEPES, 1% non-essential amino acid, and 0.1% β-mercaptoethanol).

For flow cytometry analysis, tumor and liver tissue samples were cut into approximately 1 mm³ pieces in RPMI-1640 medium with 10% fetal bovine serum and enzymatically digested using the MACS tumor dissociation kit for mouse (Miltenyi Biotec, 130-096-730) for 30 min on a rotor at 37 °C, according to the manufacturer's instructions. After being filtered through a 70 μm Cell-Strainer in RPMI-1640 medium, the suspended cells were centrifuged at 300×g for 3 min and purified by percoll-gradient centrifugation. The immune cells were suspended in red blood cell lysis buffer and incubated on ice for 3 min to lyse red blood cells. The cell pellets were re-suspended in sorting buffer (PBS supplemented with 2% FBS) after washing twice with PBS for further staining and flow cytometry analysis. For intracellular cytokines staining (Granzyme B⁺CD8⁺ T cells, IFN-γ⁺CD8⁺ T cells), cells were stimulated with 100 ng/mL PMA and 500 ng/mL ionomycin in the presence of 3 μg/mL brefeldin A for 4 h before staining with antibodies against surface proteins, followed by fixation, permeabilization, and staining with indicated antibodies against intracellular antigens. Stained cells were analyzed by BD LSRFortessa. The antibodies used in this paper are listed in Table S6.

RNA fluorescence in situ hybridization
Cy3-conjugated *HDAC2-AS2* probes were used for FISH assay and designed by the Stellaris FISH Probe Designer (Biosearch Technologies). Briefly, CD8⁺ T cells were fixed in 4% formaldehyde plus 10% acetic acid in PBS for 15 min at room temperature, then were permeabilized in PBS plus 0.5% Triton X-100 and 10 mM Ribonucleoside Vanadyl Complexes (RVC) for 10 min on ice. Hybridization was carried out by following the Biosearch Technologies protocol. Cells were further incubated with rabbit anti-CDK9 antibody followed by Alexa Fluor 488 anti-rabbit secondary antibody. Images were obtained in the Zeiss LSM700 laser-scanning confocal microscope.

LncRNA microarray analysis
The custom-designed microarray platform was utilized as described previously[73]. Briefly, RNA expression profiling was conducted using the Agilent human microarray V.4.0 platform, consisting of probes for 21,789 protein-coding genes and 39,311 lncRNA transcripts. At least one probe was designed for each lncRNA transcript. Subsequently, quantile normalization and data processing were performed using Agilent Gene Spring Software. All microarray datasets have been deposited at the Gene Expression Omnibus (GEO) under accession number GSE197220.

Analysis of single-cell RNA-seq datasets
The expression matrices of scRNA-seq datasets and related metadata of patients with liver cancer were obtained from GEO: GSE151530 (GEO), GSE149614 (GEO), and GSE98638 (GEO). The T cells were included in the analysis of cluster assignments and trajectory construction using Seurat v4.3.0 and monocle2. For further differential gene expression analysis of CDK9⁺CD8⁺ T cells, we assigned each T cell with Transcripts Per Million (TPM) of CD8A/CD4 >3 to the CD8⁺ T cell and that with TPM of CD4/CD8A >3 to the CD4⁺ T cell, while filtering out other T cells. Then we sub-grouped the T cells into CDK9⁺ (TPM > 0) and CDK9⁻ (TPM = 0), and performed gene enrichment between the CDK9⁻CD8⁺ and CDK9⁺CD8⁺ T cells, as well as CDK9⁻CD4⁺ and CDK9⁺CD4⁺ T cells. The top elevated 200 genes enriched in CDK9⁺CD8⁺ T cells were subjected to Metascape analysis.

Analysis of single-cell Ti-ATAC-seq 2 dataset
The published single-cell Ti-ATAC-seq 2 dataset of HCC were analyzed using ArchR as previously reported[44,74], including dimensionality reduction, UMAP projection, identification of marker features. The chromatin accessibility of CDK9 as indicated by the gene score was measured for each cluster. And the clonal expansion as indicated by the clonotype size of T cells was calculated and compared within CD8⁺ T-cell clusters.

TCGA data analysis
We used R packages "TCGAbiolinks" to download the gene expression data and associated clinical data from TCGA-LIHC project. The gene expression matrix among the patients was normalized by the R package "DESeq2". The mean expression of each gene in the tumor was used to group patients into high and low groups. We used the R package "survival" to perform the statistical analysis.

Statistical analysis
Unless otherwise indicated, data are presented as mean ± SEM of three independent experiments. GraphPad Software was used for data analysis. The two-tailed Student's *t*-test was used to compare gene expression between two selected groups. The correlation between gene expressions was analyzed using Pearson's test. Two-way ANOVA was used to analyze the tumor growth.

Reporting summary
Further information on research design is available in the Nature Portfolio Reporting Summary linked to this article.

Data availability
The microarray datasets have been deposited at the Gene Expression Omnibus (GEO) under accession number GSE197220. The previously published data are available under the accession numbers HRA010216 (National Genomic Data Center, bioProject accession PRJCA007947: https://ngdc.cncb.ac.cn/search/specific?db=hra&q=HRA010216+), GSE151530 (GEO: https://www.ncbi.nlm.nih.gov/geo/query/acc.cgi?acc=GSE151530), GSE149614 (GEO: https://www.ncbi.nlm.nih.gov/geo/query/acc.cgi?acc=GSE149614), GSE98638 (GEO: https://www.ncbi.nlm.nih.gov/geo/query/acc.cgi?acc=GSE98638). All other data supporting the findings of this study are available from the corresponding authors on reasonable request. Source data are provided with this paper.

Code availability
Codes used in this study are posted on GitHub for main analysis (https://github.com/YouMaojun/CDK9-CD8-T-cells).

References
1. Sung, H. et al. Global Cancer Statistics 2020: GLOBOCAN estimates of incidence and mortality worldwide for 36 cancers in 185 countries. *CA Cancer J. Clin.* **71**, 209–249 (2021).

2. Forner, A., Reig, M. & Bruix, J. Hepatocellular carcinoma. *Lancet* **391**, 1301–1314 (2018).

3. Llovet, J. M. et al. Hepatocellular carcinoma. *Nat. Rev. Dis. Prim.* **7**, 6 (2021).

4. Yoh, T. et al. Surgery for recurrent hepatocellular carcinoma: achieving long-term survival. *Ann. Surg.* **273**, 792–799 (2021).

5. Kulik, L. & El-Serag, H. B. Epidemiology and management of hepatocellular carcinoma. *Gastroenterology* **156**, 477–491.e471 (2019).

6. Yang, P. et al. TGF-beta-miR-34a-CCL22 signaling-induced Treg cell recruitment promotes venous metastases of HBV-positive hepatocellular carcinoma. *Cancer Cell* **22**, 291–303 (2012).

7. Zheng, X., Jin, W., Wang, S. & Ding, H. Progression on the roles and mechanisms of tumor-infiltrating T lymphocytes in patients with hepatocellular carcinoma. *Front. Immunol.* **12**, 729705 (2021).

8. Fu, J. et al. Increased regulatory T cells correlate with CD8 T-cell impairment and poor survival in hepatocellular carcinoma patients. *Gastroenterology* **132**, 2328–2339 (2007).

9. Wang, J. et al. Tumor-infiltrated CD8+ T Cell 10-gene signature related to clear cell renal cell carcinoma prognosis. *Front. Immunol.* **13**, 930921 (2022).

10. Jaiswal, A. et al. An activation to memory differentiation trajectory of tumor-infiltrating lymphocytes informs metastatic melanoma outcomes. *Cancer Cell* **40**, 524–544.e525 (2022).

11. Zhou, G. et al. Antibodies against immune checkpoint molecules restore functions of tumor-infiltrating T cells in hepatocellular carcinomas. *Gastroenterology* **153**, 1107–1119.e1110 (2017).

12. Kopp, F. & Mendell, J. T. Functional classification and experimental dissection of long noncoding RNAs. *Cell* **172**, 393–407 (2018).

13. Wong, C. M., Tsang, F. H. & Ng, I. O. Non-coding RNAs in hepatocellular carcinoma: molecular functions and pathological implications. *Nat. Rev. Gastroenterol. Hepatol.* **15**, 137–151 (2018).

14. Wang, Y. L. et al. Lnc-UCID promotes G1/S transition and hepatoma growth by preventing DHX9-mediated CDK6 down-regulation. *Hepatology* **70**, 259–275 (2019).

15. Zhang, Y., Luo, M., Cui, X., O'Connell, D. & Yang, Y. Long non-coding RNA NEAT1 promotes ferroptosis by modulating the miR-362-3p/MIOX axis as a ceRNA. *Cell Death Differ.* **29**, 1850–1863 (2022).

16. Tseng, Y. Y. et al. PVT1 dependence in cancer with MYC copy-number increase. *Nature* **512**, 82–86 (2014).

17. Yuan, J. H. et al. A long noncoding RNA activated by TGF-beta promotes the invasion-metastasis cascade in hepatocellular carcinoma. *Cancer Cell* **25**, 666–681 (2014).

18. Liu, J. et al. CCR7 chemokine receptor-inducible lnc-Dpf3 restrains dendritic cell migration by inhibiting HIF-1alpha-mediated glycolysis. *Immunity* **50**, 600–615.e615 (2019).

19. Li, G. et al. LIMIT is an immunogenic lncRNA in cancer immunity and immunotherapy. *Nat. Cell Biol.* **23**, 526–537 (2021).

20. Fasolo, F. et al. Long noncoding RNA MIAT controls advanced atherosclerotic lesion formation and plaque destabilization. *Circulation* **144**, 1567–1583 (2021).

21. Wang, Y. et al. Decreased expression of the host long-noncoding RNA-GM facilitates viral escape by inhibiting the kinase activity TBK1 via S-glutathionylation. *Immunity* **53**, 1168–1181.e1167 (2020).

22. Jiang, R. Q. et al. The long noncoding RNA lnc-EGFR stimulates T-regulatory cells differentiation thus promoting hepatocellular carcinoma immune evasion. *Nat. Commun.* **8**, 15129 (2017).

23. Huang, D. et al. NKILA lncRNA promotes tumor immune evasion by sensitizing T cells to activation-induced cell death. *Nat. Immunol.* **19**, 1112–1125 (2018).

24. Das, S. et al. The extracellular RNA Communication Consortium: establishing foundational knowledge and technologies for extracellular RNA research. *Cell* **177**, 231–242 (2019).

25. Luo, C. et al. Tumor-derived exosomes induce immunosuppressive macrophages to foster intrahepatic cholangiocarcinoma progression. *Hepatology* **76**, 982–999 (2022).

26. Morrissey, S. M. et al. Tumor-derived exosomes drive immunosuppressive macrophages in a pre-metastatic niche through glycolytic dominant metabolic reprogramming. *Cell Metab.* **33**, 2040 (2021).

27. Chen, J. H. et al. GOLM1 exacerbates CD8 T cell suppression in hepatocellular carcinoma by promoting exosomal PD-L1 transport into tumor-associated macrophages. *Signal Transduct. Target. Ther.* **6**, 397 (2021).

28. Wang, Z. et al. Extracellular vesicles in fatty liver promote a metastatic tumor microenvironment. *Cell Metab.* **35**, 1209–1226.e1213 (2023).

29. Kalluri, R. & McAndrews, K. M. The role of extracellular vesicles in cancer. *Cell* **186**, 1610–1626 (2023).

30. Chen, F. et al. Extracellular vesicle-packaged HIF-1alpha-stabilizing lncRNA from tumour-associated macrophages regulates aerobic glycolysis of breast cancer cells. *Nat. Cell Biol.* **21**, 498–510 (2019).

31. Li, Z. et al. Glioblastoma cell-derived lncRNA-containing exosomes induce microglia to produce complement C5, promoting chemotherapy resistance. *Cancer Immunol. Res.* **9**, 1383–1399 (2021).

32. Huang, Y. et al. Exosomal lncRNA SNHG10 derived from colorectal cancer cells suppresses natural killer cell cytotoxicity by upregulating INHBC. *Cancer Cell Int.* **21**, 528 (2021).

33. Massague, J. TGFbeta in cancer. *Cell* **134**, 215–230 (2008).

34. Matsuzaki, K. Modulation of TGF-beta signaling during progression of chronic liver diseases. *Front. Biosci.* **14**, 2923–2934 (2009).

35. Yan, H. et al. Sodium taurocholate cotransporting polypeptide is a functional receptor for human hepatitis B and D virus. *Elife* **1**, e00049 (2012).

36. Costa-Silva, B. et al. Pancreatic cancer exosomes initiate pre-metastatic niche formation in the liver. *Nat. Cell Biol.* **17**, 816–826 (2015).

37. Peinado, H. et al. Melanoma exosomes educate bone marrow progenitor cells toward a pro-metastatic phenotype through MET. *Nat. Med.* **18**, 883–891 (2012).

38. Liu, Y. et al. Tumor exosomal RNAs promote lung pre-metastatic niche formation by activating alveolar epithelial TLR3 to recruit neutrophils. *Cancer Cell* **30**, 243–256 (2016).

39. Mandal, R., Becker, S. & Strebhardt, K. Targeting CDK9 for anti-cancer therapeutics. *Cancers (Basel)* **13**, 2181 (2021).

40. Bacon, C. W. & D'Orso, I. CDK9: a signaling hub for transcriptional control. *Transcription* **10**, 57–75 (2019).

41. Napolitano, G., Licciardo, P., Carbone, R., Majello, B. & Lania, L. CDK9 has the intrinsic property to shuttle between nucleus and cytoplasm, and enhanced expression of cyclin T1 promotes its nuclear localization. *J. Cell Physiol.* **192**, 209–215 (2002).

42. Napolitano, G., Majello, B. & Lania, L. Catalytic activity of Cdk9 is required for nuclear co-localization of the Cdk9/cyclin T1 (P-TEFb) complex. *J. Cell Physiol.* **197**, 1–7 (2003).

43. Chen, E. W., Tay, N. Q., Brzostek, J., Gascoigne, N. R. J. & Rybakin, V. A dual inhibitor of Cdc7/Cdk9 potently suppresses T cell activation. *Front. Immunol.* **10**, 1718 (2019).

44. You, M. et al. Epigenetic regulation of HBV-specific tumor-infiltrating T cells in HBV-related HCC. *Hepatology* **78**, 943–958 (2023).

45. Ma, L. et al. Single-cell atlas of tumor cell evolution in response to therapy in hepatocellular carcinoma and intrahepatic cholangiocarcinoma. *J. Hepatol.* **75**, 1397–1408 (2021).

46. Zheng, C. et al. Landscape of infiltrating T cells in liver cancer revealed by single-cell sequencing. *Cell* **169**, 1342–1356.e1316 (2017).

47. Bistrović, A. et al. Synthesis and anti-proliferative effects of mono- and bis-purinomimetics targeting kinases. *Int. J. Mol. Sci.* **18**, 2292 (2017).

48. Pokhrel, R. H. et al. AMPK promotes antitumor immunity by down-regulating PD-1 in regulatory T cells via the HMGCR/p38 signaling pathway. *Mol. Cancer* **20**, 133 (2021).

49. Lu, Y. et al. A single-cell atlas of the multicellular ecosystem of primary and metastatic hepatocellular carcinoma. *Nat. Commun.* **13**, 4594 (2022).

50. Wang, J. et al. Crosstalk between transforming growth factor-beta signaling pathway and long non-coding RNAs in cancer. *Cancer Lett.* **370**, 296–301 (2016).

51. Chen, K. et al. lncRNA DLGAP1-AS2 Knockdown Inhibits Hepato-cellular Carcinoma Cell Migration and Invasion by Regulating miR-154-5p Methylation. *Biomed. Res. Int.* **2020**, 6575724 (2020).

52. Miao, W. et al. LncRNA DLGAP1-AS2 modulates glioma development by up-regulating YAP1 expression. *J. Biochem.* **167**, 411–418 (2020).

53. Xu, H. & Cao, X. Dendritic cell vaccines in cancer immunotherapy: from biology to translational medicine. *Front. Med.* **5**, 323–332 (2011).

54. Andreola, G. et al. Induction of lymphocyte apoptosis by tumor cell secretion of FasL-bearing microvesicles. *J. Exp. Med.* **195**, 1303–1316 (2002).

55. Huber, V. et al. Human colorectal cancer cells induce T-cell death through release of proapoptotic microvesicles: role in immune escape. *Gastroenterology* **128**, 1796–1804 (2005).

56. Taylor, D. D., Gercel-Taylor, C., Lyons, K. S., Stanson, J. & Whiteside, T. L. T-cell apoptosis and suppression of T-cell receptor/CD3-zeta by Fas ligand-containing membrane vesicles shed from ovarian tumors. *Clin. Cancer Res.* **9**, 5113–5119 (2003).

57. Clayton, A. et al. Human tumor-derived exosomes down-modulate NKG2D expression. *J. Immunol.* **180**, 7249–7258 (2008).

58. Szajnik, M., Czystowska, M., Szczepanski, M. J., Mandapathil, M. & Whiteside, T. L. Tumor-derived microvesicles induce, expand and up-regulate biological activities of human regulatory T cells (Treg). *PLoS ONE* **5**, e11469 (2010).

59. Valenti, R. et al. Human tumor-released microvesicles promote the differentiation of myeloid cells with transforming growth factor-beta-mediated suppressive activity on T lymphocytes. *Cancer Res.* **66**, 9290–9298 (2006).

60. Takov, K., Yellon, D. M. & Davidson, S. M. Confounding factors in vesicle uptake studies using fluorescent lipophilic membrane dyes. *J. Extracell. Vesicles* **6**, 1388731 (2017).

61. Munter, R. et al. Dissociation of fluorescently labeled lipids from liposomes in biological environments challenges the interpretation of uptake studies. *Nanoscale* **10**, 22720–22724 (2018).

62. Simonsen, J. B. Pitfalls associated with lipophilic fluorophore staining of extracellular vesicles for uptake studies. *J. Extracell. Vesicles* **8**, 1582237 (2019).

63. Wherry, E. J. & Kurachi, M. Molecular and cellular insights into T cell exhaustion. *Nat. Rev. Immunol.* **15**, 486–499 (2015).

64. MacLachlan, T. K. et al. Binding of CDK9 to TRAF2. *J. Cell. Biochem.* **71**, 467–478 (1998).

65. Beauchamp, E. M. et al. Identification and targeting of novel CDK9 complexes in acute myeloid leukemia. *Blood* **133**, 1171–1185 (2019).

66. Mita, M. M. et al. Phase 1 safety, pharmacokinetic and pharmaco-dynamic study of the cyclin-dependent kinase inhibitor dinaciclib administered every three weeks in patients with advanced malig-nancies. *Br. J. Cancer* **117**, 1258–1268 (2017).

67. Benson, C. et al. A phase I trial of the selective oral cyclin-dependent kinase inhibitor seliciclib (CYC202; R-Roscovitine), administered twice daily for 7 days every 21 days. *Br. J. Cancer* **96**, 29–37 (2007).

68. Mita, M. M. et al. Randomized Phase II Trial of the cyclin-dependent kinase inhibitor dinaciclib (MK-7965) versus capecitabine in patients with advanced breast cancer. *Clin. Breast Cancer* **14**, 169–176 (2014).

69. Mitri, Z. et al. A phase 1 study with dose expansion of the CDK inhibitor dinaciclib (SCH 727965) in combination with epirubicin in patients with metastatic triple negative breast cancer. *Investig. N. Drugs* **33**, 890–894 (2015).

70. Murphy, A. G. et al. A Phase I Study of dinaciclib in combination with MK-2206 in patients with advanced pancreatic cancer. *Clin. Transl. Sci.* **13**, 1178–1188 (2020).

71. Tsai, M. C. et al. Long noncoding RNA as modular scaffold of histone modification complexes. *Science* **329**, 689–693 (2010).

72. Thery, C., Amigorena, S., Raposo, G. & Clayton, A. Isolation and characterization of exosomes from cell culture supernatants and biological fluids. *Curr. Protoc. Cell Biol.* **Chapter 3**(Unit 3), 22 (2006).

73. Yuan, J. et al. Transcriptional profiling analysis and functional pre-diction of long noncoding RNAs in cancer. *Oncotarget* **7**, 8131–8142 (2016).

74. You, M. et al. Single-cell epigenomic landscape of peripheral immune cells reveals establishment of trained immunity in indivi-duals convalescing from COVID-19. *Nat. Cell Biol.* **23**, 620–630 (2021).

Acknowledgements

Author contributions

Conceptualization: P.Y., R.C., J.L., Y.G., and Z.Z.; methodology: Y.G., Z.Z., X.H., M.Y., X.D., and J.L.; investigation: Y.G., Z.Z., X.H., M.Y., C.D., J.L., Y.H., and X.D.; resources: N.L., K.W., and S.C.; writing—original draft: P.Y., Y.G., Z.Z., X.H., and M.Y.; writing—review and editing: all authors; supervision: P.Y., R.C., J.L., S.C. and F.Y.; funding acquisition: P.Y., Y.G., and M.Y.

Competing interests

The authors declare no competing interests.

Additional information